

Detecting isotopologues in exoplanet atmospheres using ground-based high-dispersion spectroscopy

P. Mollière¹ and I.A.G. Snellen¹

Leiden Observatory, Leiden University, Postbus 9513, 2300 RA Leiden, The Netherlands

Received 31 August 2018 / Accepted –

ABSTRACT

Context. The cross-correlation technique is a well-tested method for exoplanet characterization, having lead to the detection of various molecules, and to constraints on atmospheric temperature profiles, wind speeds, and planetary spin rates. A new, potentially powerful application of this technique is the measurement of atmospheric isotope ratios. In particular D/H ratios can give unique insights in the formation and evolution of planets and their atmospheres.

Aims. In this paper we aim to study the detectability of molecular isotopologues in the high-dispersion spectra of exoplanet atmospheres, to identify the optimal wavelength ranges to conduct such studies, and to predict the required observational efforts - both with current and future ground-based instrumentation.

Methods. High-dispersion ($R=100,000$) thermal emission spectra, and in some cases reflection spectra, are simulated by self-consistent modelling of the atmospheric structures and abundances of exoplanets over a wide range of effective temperatures. These are synthetically observed with a telescope equivalent to the VLT and/or ELT, and analysed using the cross-correlation technique, resulting in signal-to-noise predictions for the ^{13}CO , HDO, and CH_3D isotopologues.

Results. We find that for the best observable exoplanets, ^{13}CO is well in range of current telescopes. We predict it will be most favourably detectable at 4.7 micron, but it should also be observable at 2.4 micron, just longward of the wavelength regions probed by several high-dispersion spectroscopic observations presented in the literature. CH_3D can be best targeted at 4.7 micron, and may also be detectable using present-day instruments for planets below 700 K in equilibrium temperature. For both isotopologues, ELT-class telescopes will allow detections for a wide range of planets. HDO is best targeted at 3.7 micron, but is more challenging, partly because methane can shield HDO absorption. However, methane-quenching may make HDO even easier to detect than CH_3D , out to temperatures ≤ 1200 K. We estimate that if Proxima Cen b is water-rich, the HDO isotopologue could be detected with the ELT in ~ 1 night of observing time in its reflected-light spectrum.

Conclusions. Isotopologues will soon be a part of the exoplanet characterisation tools. Measuring D/H ratios in exoplanets, and that of other isotopologues, could become a prime science case for the first-light instrument *METIS* on the European ELT, especially for nearby temperate rocky and ice giant planets. This can provide unique insights in their history of, e.g., icy-body enrichment and atmospheric evaporation processes.

Key words. methods: numerical – planets and satellites: atmospheres – radiative transfer

1. Introduction

The cross-correlation technique is a well established tool for detecting the presence of molecular absorbers in exoplanet atmospheres. In addition, it can constrain a planet's atmospheric temperature profile, planetary spin rate and wind patterns, as well as its mass – in the case of a non-transiting planet. Examples are the detection of CO in HD 209458 b (which also constrained the planet's wind speed, see [Snellen et al. 2010](#)), CO in β Pic b (which also constrained the planet's spin rate, see [Snellen et al. 2014](#)), CO in τ Boötis b ([Brogi et al. 2012](#); [Rodler et al. 2012](#)), H_2O in 51 Peg b ([Birkby et al. 2017](#)), H_2O in HD 88133 b and Ups And b ([Piskorz et al. 2016, 2017](#)), H_2O and CO in HD 179949 b ([Brogi et al. 2014](#)), H_2O ([Birkby et al. 2013](#)) and CO in HD 189733b ([Rodler et al. 2013](#); [de Kok et al. 2013](#)), and TiO in the temperature-inverted part of WASP-33b's atmosphere ([Nugroho et al. 2017](#)). [Bryan et al. \(2018\)](#) measured the rotation rates for a set of planets and brown dwarfs by cross-correlating with atmospheric models containing, among others, H_2O and CO opacities. Recently, atomic and ionized species were de-

tected using cross-correlation techniques in the optical transmission spectrum of the hottest known planet Kelt-9b ([Hoeijmakers et al. 2018](#)).

In the study presented here, we investigate how the cross-correlation technique may be used to identify isotopologues in planetary atmospheres. Isotopologues are molecular chemical species with different numbers of neutrons in the nuclei of their constituent atoms. We study the feasibility of such a detection using current and next-generation instruments, in particular *CRISP*+ ([Follert et al. 2014](#)) on the Very Large Telescope, and *METIS* ([Brandl et al. 2014](#)) on the ELT.

Most of the near-infrared (NIR) molecular opacity of (hot) Jupiters originates from H-, C- and O- bearing species. In this study, we therefore concentrate on the isotopologues of CO, H_2O and CH_4 . H_2O and CH_4 are expected to be abundant in temperate, low-mass planets, with H_2O playing a key role in planet habitability. Isotopologue detections and subsequent measurements of isotop(ologu)e-ratios from these species can provide interesting insights in planet formation and atmospheric processes. In principle, this requires benchmarking the inferred ratios with those observed in the host star or the surrounding interstellar medium. Although there exists scatter in our local neighborhood

Send offprint requests to: Paul MOLLIÈRE, e-mail: molliere@strw.leidenuniv.nl

(~ 1 kpc), the carbon, oxygen and hydrogen isotope ratio variations are usually not larger than a factor of a few (see, e.g., Milam et al. 2005; Polehampton et al. 2005; Linsky et al. 2006).¹ Hence, if exoplanet isotope ratios are found to be very different from the average local ISM values, this would make the planet stand out already without having to compare to the isotope ratios of its host star.

Typical isotope ratios in the neighborhood of the sun are $^{12}\text{C}/^{13}\text{C} \sim 50$ (Milam et al. 2005), $^{16}\text{O}/^{17}\text{O} \sim 1600$ (Romano et al. 2017), $^{16}\text{O}/^{18}\text{O} \sim 400$ (Polehampton et al. 2005), and deuterium to hydrogen (D/H) $\sim 2 \times 10^{-5}$ (Linsky et al. 2006; Asplund et al. 2009). Note that in the solar system the oxygen and carbon isotope ratios are $\sim 30\%$ larger, probably because the sun formed 4.5 Gyr ago, conserving the higher isotope ratios from that period (Clayton & Nittler 2004; Ayres et al. 2013).

1.1. Isotopologues and planet formation

Variations in the isotope ratios may provide clues on how planets form from the condensed and gaseous material in proto-planetary disks. In the solar system, such variations are most prominent in the D/H ratio (see Figure 1 of Altwegg et al. 2015). Volatile-rich primitive meteorites are found to be enriched in D by about a factor 6 compared to the proto-solar nebula. This enrichment is found to be comparable or higher for Jupiter-family comets, and to be a factor 10–20 for Oort-cloud comets, although significant scatter exists. This trend of enrichment in D within the condensed volatiles appears to increase with distance from the Sun. This may be explained by a temperature-dependent fractionation of D into water ice (see, e.g., Geiss & Reeves 1981), but note that the Oort comets may have formed in the inner Solar System, and then been scattered outward by the giant planets (see, e.g., Morbidelli 2005, and the references therein).

The gas giants Jupiter and Saturn are found to have D/H ratios of $(2.6 \pm 0.7) \times 10^{-5}$ and $1.7^{+0.75}_{-0.45} \times 10^{-5}$ respectively (Mahaffy et al. 1998; Lellouch et al. 2001), roughly in line with the proto-solar value (2×10^{-5}). In contrast, the ice giants Uranus and Neptune have measured ratios of $(4.4 \pm 0.4) \times 10^{-5}$ and $(4.1 \pm 0.4) \times 10^{-5}$ (Feuchtgruber et al. 2013), hence they are D-enriched by a factor of ~ 2 . This is thought to be caused by atmospheric contamination by icy planetesimals. While the fraction of such contamination is low for Jupiter and Saturn, having no effect on their D/H ratio, this is significant for Uranus and Neptune. Assuming that these icy planetesimals had an intrinsic D/H enrichment of an order of magnitude, like that of comets (i.e. $\text{D}/\text{H} \sim 2 \times 10^{-4}$), and assuming an atmospheric enrichment as indicated by Guillot & Gautier (2014) for Uranus and Neptune, it can have caused the overall D-enrichment of their atmospheres by a factor of two.

However, it is not yet known whether this scheme generally applies to planet formation processes. Numerous studies address atmospheric composition (relative to H/He), and its connection to a planet's formation history, often assuming that it is governed by gas that the planet accretes, instead of planetesimals (Öberg et al. 2011; Ali-Dib et al. 2014; Thiabaud et al. 2014; Helling et al. 2014; Marboeuf et al. 2014b,a; Madhusudhan et al. 2014;

Mordasini et al. 2016; Öberg & Bergin 2016; Madhusudhan et al. 2016; Cridland et al. 2016). Among these Mordasini et al. (2016) is a notable exception, assuming planetesimal, rather than gas enrichment. In the case of gas enrichment, volatiles in the gas phase of the disk are expected to be partly sequestered into condensates, resulting in lower metallicities but unchanged isotopologue ratios in the disk gas. Hence, it is expected that isotopologue ratios in the atmospheres of extrasolar planets will not be significantly different from that of their host stars or local ISM, except if they are strongly contaminated by icy planetesimals, which have increased D/H ratios. The inferred trends of increasing planetary bulk metallicity as a function of decreasing planetary mass may be seen as a sign of planetesimal / solid body enrichment dominating over gas enrichment (Miller & Fortney 2011; Thorngren et al. 2016). Recently, synthetic planet formation calculations by Marboeuf et al. (2018) have been able to reproduce the planetary mass – D/H correlation in the Solar System, when applying the envelope pollution by planetesimals as advocated by Mordasini et al. (2016).

In contrast to deuterium/hydrogen, there is no evidence for strong fractionation of either oxygen or carbon. The $^{16}\text{O}/^{18}\text{O}$ values inferred from comets such as 1P/Halley, 67P/Churyumov-Gerasimenko and C/2014 Q2 (Lovejoy) (see Altwegg & Bockelée-Morvan 2003; Altwegg et al. 2015; Biver et al. 2016, and the references therein) are broadly consistent with the galactic abundances compiled by (Romano et al. 2017). The same holds for the oxygen isotopic abundances of primitive and differentiated meteorites (systematic variations do exist, but only of the order of single digit percentage values, see, e.g., Clayton 1993; Yurimoto et al. 2007). Also, the $^{12}\text{C}/^{13}\text{C}$ ratios observed in 11 different comets (see Altwegg & Bockelée-Morvan 2003; Biver et al. 2016, and the references therein) and chondrites of different types (see, e.g., Halbout et al. 1986; Pearson et al. 2006) are all consistent with the galactic values inferred in Milam et al. (2005). This means that neither C nor O condensates have a significant preference for a certain isotope, resulting in the gas and condensate phase C and O isotope ratios to be unaffected, at least down to a percentage level (e.g., Clayton 1993; Yurimoto et al. 2007).

1.2. Isotopologues and atmospheric escape

A process which can further affect the D/H ratio is atmospheric escape: thermal or ion pick-up escape processes preferentially retain more massive isotopologues (see, e.g. Jakosky & Phillips 2001). Hence D is expected to be relatively more abundant than H in planets which have undergone significant (non-hydrodynamic) atmospheric loss. This seems to be indeed the case for Mars, which exhibits a D/H ratio of at least 5–7 times larger than the terrestrial value (see, e.g., Krasnopolsky 2015; Villanueva et al. 2015; Clarke et al. 2017). The primordial value inferred for Mars is about twice the terrestrial value (Leshin 2000). Identifying water as the major hydrogen carrier, the above values correspond to equivalent ocean depths between at least 60 and 130 m having been lost from the Martian surface (Krasnopolsky 2015; Villanueva et al. 2015). For Venus the process of evaporation may have been even more extreme, because its atmospheric D/H ratio is about 1000 times higher than the protosolar value of 2×10^{-5} (Kulikov et al. 2006).

¹ Note that for carbon and oxygen the isotopic ratios $^{12}\text{C}/^{13}\text{C}$, $^{16}\text{O}/^{17}\text{O}$ and $^{16}\text{O}/^{18}\text{O}$ are decreasing toward the galactic center (see, e.g., Milam et al. 2005; Romano et al. 2017). This is thought to be caused by dredge-up of heavier C and O isotopes as reaction-intermediates of the CNO cycle in AGB stars, which are later ejected into the ISM with the stars' outer layers.

1.2.1. Isotopologues and biology

There is also a particularly interesting prospect that isotopologue measurements could shed light on biological processes and help to provide evidence for the presence of extraterrestrial life. Living matter on Earth tends to favour ^{12}C over ^{13}C when building organic carbon molecules: for organic carbon compounds the $^{13}\text{C}/^{12}\text{C}$ ratio is 3 % lower than for inorganic compounds (see, e.g., Langmuir & Broecker 2012, and the references therein). For Earth, the absolute $^{13}\text{C}/^{12}\text{C}$ values in the organic and inorganic reservoirs depend on the fractionation of carbon between these two reservoirs, as well as on the total $^{13}\text{C}/^{12}\text{C}$ (crustal) average. A possible tracer of life would thus be to compare the $^{13}\text{C}/^{12}\text{C}$ ratios of atmospheric methane (mostly organic origin on Earth, see, e.g., Quay et al. 1991) and CO_2 (inorganic origin, if not derived from burning fossil fuels, see, e.g., Ghosh & Brand 2003). Alternatively, if the $^{13}\text{C}/^{12}\text{C}$ crustal average of a terrestrial exoplanet was known, and the $^{13}\text{C}/^{12}\text{C}$ in its oxidized (e.g. CO , CO_2) or reduced (CH_4) atmospheric components could be measured, then the carbon fractionation into organic (i.e. living, or recently living) matter could be inferred. However, assuming these processes would be the same as on Earth, these effects are very difficult to measure, requiring a precision in absolute ^{13}C abundance of $\sim 10^{-4}$. For exoplanets, we expect this to be out of scope of any present or future planned instrument or telescope.

In this paper, we focus on the detectability of carbon monoxide (^{13}CO), methane (CH_3D) and water (HDO), because we expect (^{13}CO) the least difficult to measure, and CH_3D and HDO to bear the greatest significance when seeking to probe a planet's formation and evolution history. In Section 2 we describe how the planetary high-resolution spectra are modeled, and how the observations are simulated. In Section 3 we present our calculations for the detectability of ^{13}CO in hot Jupiters, as a function of wavelength. In Section 4 we show how HDO may be found in self-luminous planets, as a function of effective temperature, with and without methane quenching in the atmosphere. In Section 5 we study the detectability of CH_3D , with the same planetary setup. Finally, the case of HDO in terrestrial exoplanet atmospheres is studied in Section 6, where we assume a twin Earth as an input model for Proxima Cen b. Our results are summarised and discussed in Section 7.

2. Model description

2.1. Atmospheric structure

The atmospheric temperature and abundance structures used to generate the high resolution spectra are derived from self-consistent atmospheric models. In the calculations presented here, structures are obtained with *petitCODE* (Mollière et al. 2015, 2017), except for the results shown in Section 6. *petitCODE* calculates the atmospheric structures of exoplanets in 1-d in radiative-convective and chemical equilibrium. The radiative transfer considers both absorption and scattering processes. Only gas opacities are considered in the calculations presented here, but clouds can optionally be included in *petitCODE* calculations, in a self-consistent fashion. The gas opacity species considered here are H_2O , CO , CO_2 , OH (HITEMP, see Rothman et al. 2010), CH_4 , NH_3 , PH_3 , HCN (ExoMol, see Tennyson & Yurchenko 2012), as well as H_2 , H_2S , C_2H_2 (HITRAN, see Rothman et al. 2013), Na , K (VALD3, see Piskunov et al. 1995), and CIA of H_2 – H_2 and H_2 – He (Borysow & Frommhold 1989; Borysow et al. 1989; Richard et al. 2012). For H_2 and CO , also the UV electronic transitions by Kurucz (1993) are included,

as well as the Rayleigh scattering opacities for H_2 , He , CO_2 , CO , CH_4 and H_2O . For the cross-sections, the values reported in Dalgarno & Williams (1962) (H_2), Chan & Dalgarno (1965) (He), Snee & Ubachs (2005) (CO_2 , CO , CH_4) and Harvey et al. (1998) (H_2O) are used.

petitCODE is a well-tested tool for calculating exoplanet atmospheric structures, and has recently been benchmarked against the *ATMO* (Tremblin et al. 2015) and *Exo-REM* (Baudino et al. 2015) codes (Baudino et al. 2017). It was used for a parameter study of irradiated atmospheres (Mollière et al. 2015), and for generating predictions of exoplanet observations with *JWST* for high-priority targets (Mollière et al. 2017). Moreover, *petitCODE* enabled the atmospheric characterization of the self-luminous planet 51 Eri b (Samland et al. 2017), and constrained the atmospheric properties of several transiting exoplanets (Mancini et al. 2016b,a, 2017; Southworth et al. 2017). Finally, it connected planet formation models with synthetic atmospheric observations in Mordasini et al. (2016).

2.2. High resolution spectra

The high resolution spectra were calculated with a new radiative transfer code, based on *petitCODE*, that we report on here for the first time. It uses the same molecular opacity database as *petitCODE*, in which pressure and temperature-dependent opacities are stored at a resolution of $\nu/\Delta\nu = 10^6$. The atmospheric structure calculations in *petitCODE* are carried out at a lower resolution, making use of the correlated-k approximation (Goody et al. 1989; Lacis & Oinas 1991; Fu & Liou 1992), as described in Appendix B of Mollière et al. (2015). The new high resolution radiative transfer code presented here uses the opacity database of *petitCODE* at its intrinsic resolution, and in a line-by-line, rather than a correlated-k treatment. Identical to the capabilities of *petitCODE*, both transmission and emission spectra can be calculated. Because the work presented in this paper focuses on the high-resolution NIR to MIR emission spectra of cloudless atmospheres, scattering is currently neglected, but scattering is included in the atmospheric structure calculations, as described in Section 2.1 above.

2.3. Synthetic observations

For a given set of planet–star parameters (stellar effective temperature and radius, planetary semi-major axis, radius, mass and atmospheric composition) self-consistent atmospheric structures are calculated, and used for generating the high-resolution emission flux $F_{\text{Planet}}(\nu)$ in the planet's rest frame, where ν denotes the frequency. In order to generate the planet's signal as it would be seen by an instrument on Earth, the rest frame frequency values are first shifted according to $\nu \mapsto \nu(1 - v_{\text{rad}}/c)$, where v_{rad} is the radial velocity between the planet and the observer, and c is the speed of light. Subsequently, the host star's flux is included by adding a flat white spectrum to the planetary flux,

$$F_{\text{tot}}(\nu) = F_{\text{Planet}}(\nu) + F_*, \quad (1)$$

where the contrast between planet and star is a free parameter. We assume that the stellar lines can be perfectly removed during the data analysis. A second free parameter is the signal-to-noise-ratio (SNR) of the stellar flux, SNR_* . For convenient numerical modeling, we set $F_* = \text{SNR}_*^2$ (assuming Poisson noise), and replace $F_{\text{Planet}}(\nu)$ with $c \cdot \text{SNR}_* \cdot F_{\text{Planet}}(\nu)/\bar{F}_{\text{Planet}}$, where \bar{F}_{Planet} is the average planetary flux and c is the desired average contrast in the considered wavelength region. Subsequently, the total flux

Parameter	Value	Reference
T_*	6260 K	SI04
R_*	1.14 R_\odot	SI04 (a)
$[\text{Fe}/\text{H}]_*$	0.22	SI04
d	0.045 AU	WM07
M_{planet}	0.98 M_{J}	BdK14
R_{planet}	1.4 R_{J}	(b)
Orbital inclination i	67.7°	BdK14
Line absorbers	H ₂ O, CO ₂ , CO, CH ₄ HCN, H ₂ S, NH ₃ , H ₂ , PH ₃ , C ₂ H ₂ , OH, Na, K	(c)
Rayleigh scatterers	H ₂ , He	(c)
CIA	H ₂ -H ₂ , H ₂ -He	(c)
Elemental abundances	$[\text{Fe}/\text{H}]_{\text{planet}} = 0.83$	(d)
Chemical abundances	chemical equilibrium	(e)

Table 1. Parameters used for the self-consistent structure calculations for HD 179949b. (a): the stellar radius was inferred using the stellar mass and surface gravity reported in Santos et al. (2004). (b): HD 179949b is a non-transiting planet, hence its radius is unknown. The value chosen here corresponds to the radii typically found for planets of that mass and insolation strength (see, e.g., <http://exoplanets.org>) (c): the references for the line opacity database of *petitCODE* can be found in Section 2.1. (d): for the solar abundances we assumed the values reported by Asplund et al. (2009). For the planet’s atmospheric enrichment the solar abundances were scaled with a value that was chosen following the method described in Section 4.1 of Mollière et al. (2017). (e): we used the chemical equilibrium code described in Mollière et al. (2017). References: BdK14: Brogi et al. (2014); SI04: Santos et al. (2004); WM07: Wittenmyer et al. (2007)

$F_{\text{tot}}(\nu)$ is multiplied with a transmission model for the Earth’s atmosphere, $\mathcal{T}(\nu)$, such that the total flux that reaches the ground-based telescope is

$$F_{\text{tel}}(\nu) = \mathcal{T}(\nu)F_{\text{tot}}(\nu). \quad (2)$$

Subsequently, the spectrum is convolved to the intrinsic spectral resolution of the instrument, and binned to the wavelength steps of the instrument. Both the instrument resolution and the number of pixels per resolution element are free parameters. We follow the convention of defining the instrumental resolution $\nu/\Delta\nu$ such that $\Delta\nu$ is the full width half maximum (FWHM) of the line spread function (LSF) of the instrument’s dispersing element. We assume a Gaussian for the LSF, hence the relation between its standard deviation and the instrument resolution is $\Delta\nu = 2\sqrt{2\ln 2}\sigma$. In the following, the result of convolving and re-binning $F_{\text{tel}}(\nu)$ will be denoted \tilde{F}_{tel} , where ν' is the frequency corresponding to the instrument pixel, with the uncertainty being

$$\sigma_{\text{tel}}(\nu') = \sqrt{\tilde{F}_{\text{tel}}(\nu')}. \quad (3)$$

The final simulated observation $F_{\text{obs}}(\nu')$ is obtained by perturbing \tilde{F}_{tel} with a Gaussian with standard deviation equal to σ_{tel} .

3. ¹³CO in hot Jupiter atmospheres

The prescription for generating simulated observations described above is used for a case study of ¹³CO in a hot Jupiter atmosphere. The HD 179949b system was chosen as a benchmark. It hosts a non-transiting gas giant (discovered by Tinney et al. 2001) with an equilibrium temperature of $T_{\text{equ}} = 1519$ K (see Table 1). Ground-based high-dispersion spectroscopic observations with *CRIRES* on ESO’s Very Large Telescope (VLT)

have already shown the presence of both water (SNR = 3.9) and CO (SNR = 5.8) in the planet’s atmosphere Brogi et al. (2014).

3.1. Synthetic HD 179949b observations

A self-consistent atmospheric structure was calculated as described in Section 2.1, assuming the input parameters from Table 1. Synthetic observations consisting of 100 high-resolution observations in orbital phase from -45° to $+45^\circ$ around superior conjunction were generated as described in Sections 2.2 and 2.3, taking into account the appropriate Doppler shifts of the planetary spectrum due to the radial component of its orbital velocity, and the waxing and waning of the planet. Also, the geometric effect of the orbital inclination on the area of the visible dayside was included. The flux of the visible part of the dayside was assumed to be uniform and equal to the average dayside flux obtained from *petitCODE*, and to be zero on the nightside. For the high resolution spectra, only the line opacities of H₂O, CO₂ and CO were included, as well as H₂-H₂ and H₂-He CIA. For the planet-to-star contrast we used the values stemming from the self-consistent calculations.

The SNR_{*} as function of wavelength was calculated relative to the value at 2.3 μm following

$$\text{SNR}_*(\lambda) = \text{SNR}_*(2.3 \mu\text{m}) \cdot \sqrt{\frac{\langle F_*(\lambda) \rangle}{\langle F_*(2.3 \mu\text{m}) \rangle}}. \quad (4)$$

Here $\langle F \rangle$ denote the average fluxes in the wavelength ranges of interest. The telluric transmission model was generated using the *ESO SkyCalc*² tool (Noll et al. 2012; Jones et al. 2013), assuming a stellar altitude of 60° (airmass=2). The elevation was set to 2640 m, corresponding to the summit of Cerro Paranal. An instrument resolution of $\nu/\Delta\nu = 10^5$ was assumed with wavelength steps corresponding to 3 pixels per resolution element $\Delta\nu$.

The CO isotopologue ratios were assumed to be the same as in the HITRAN/HITEMP databases (their molparam.txt file): ¹²C¹⁶O constitutes 98.7 %, while ¹³C¹⁶O constitutes 1.1 % of all CO molecules. The HITRAN/HITEMP values are based on the compilation of telluric isotopic abundances by De Bièvre et al. (1984). Note that in the case of ¹²C/¹³C, variations in the Solar System and its neighborhood are small (as discussed in Section 1), justifying the use of the telluric values, given in Table E.1.

3.2. Analysis of the synthetic observations

For the analysis of the synthetic observations, standard methods, as have been used for real high-dispersion observations, were applied (see, e.g., Brogi et al. 2012, 2014). The main steps of the analysis are briefly described below. The data are organised as a two-dimensional matrix, where the columns represent the wavelength steps, and rows the spectra taken at different orbital phases.

1. Two data sets, A and B, are created, which are identical, except that the carbon monoxide lines of all CO isotopologues, except for ¹³C¹⁶O, and that of other spectroscopically-active molecules are removed from B: this was done by calculating planet spectra which contained all species, except the targeted ¹³C¹⁶O isotopologue. Multiplying this new spectrum

² <https://www.eso.org/observing/etc/skycalc/>

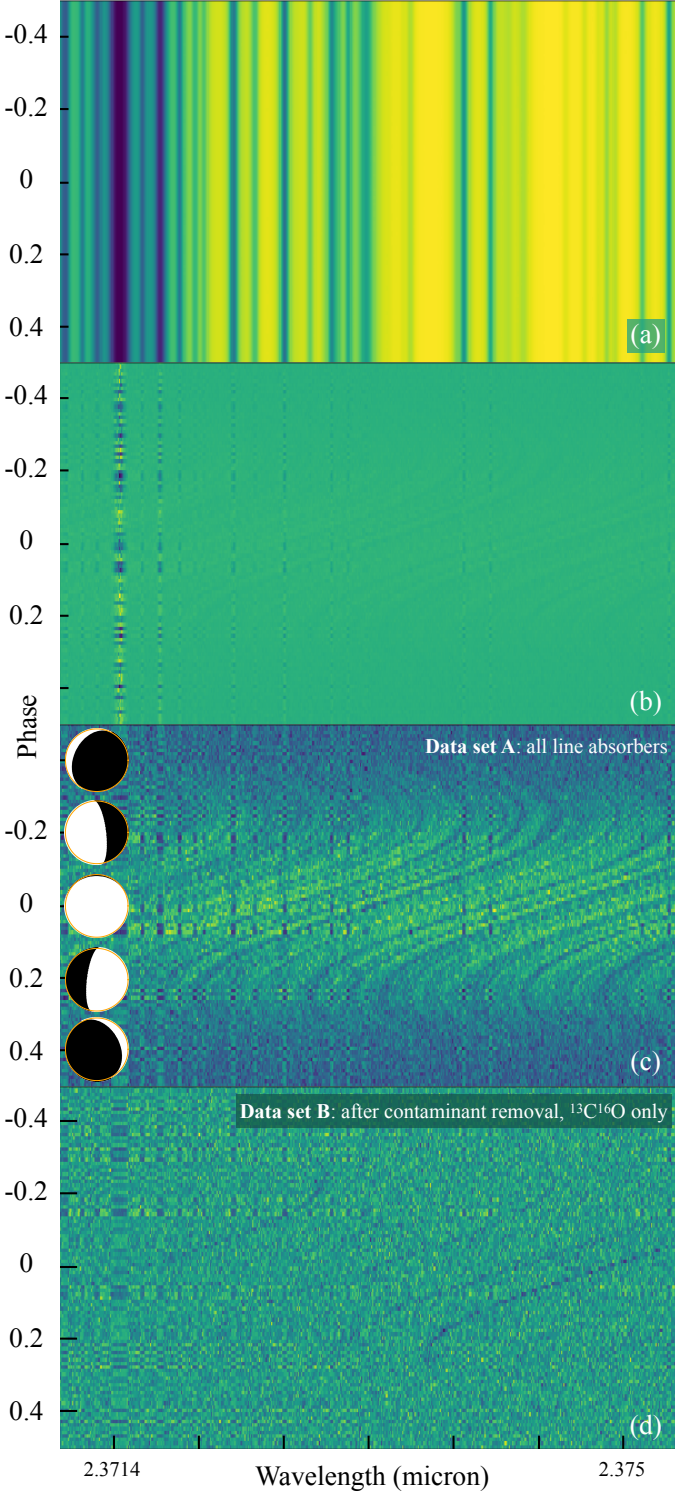


Fig. 1. Different analysis steps of the simulated observations. *Panel (a):* raw synthetic data; *Panel (b):* Data after the telluric correction; *Panel (c):* The same, after normalisation of each column by its standard deviation, this is data set A; *Panel (d):* The same as *Panel (c)*, but with the signal of the main $^{12}\text{C}^{16}\text{O}$ isotopologue and other contaminant line absorbers removed, making the lines originating from $^{13}\text{C}^{16}\text{O}$ visible. This is data set B.

with the telluric transmission model (measured from the synthetic data set A, see below, to emulate a real data analysis as closely as possible), the new spectrum was then sub-

tracted from data set A, resulting in data set B. Hence, the latter only contains the lines of the targeted $^{13}\text{C}^{16}\text{O}$. Using data set B significantly simplifies the analysis of the contribution of the $^{13}\text{C}^{16}\text{O}$ isotopologue in the spectra. For real observations, all available information on the planet spectrum, including those from other observations will be used to constrain the atmospheric structure and relative volume mixing ratios of the relevant spectroscopically-active molecules. Subsequently, spectra will need to be modeled assuming a range of isotope ratios and compared to the data. If the data are significantly better fitted by models for which the secondary isotopologue is included, this isotopologue is detected and an isotope-ratio can be inferred. In this paper, we assume that sufficient information on the planet atmosphere will be available to perform such analysis, validating our simplified approach. Hence, we do not study the retrievability of isotopologue abundances for atmospheres in which the molecular volume mixing ratios and temperature structure are not well constrained. The following steps are identical for the data sets A and B.

2. For every column the median value was calculated and used to normalise the data. This value as function of wavelength is the best estimate of the telluric absorption line spectrum, which in our simulations is kept constant throughout the observations, implying, within noise-limits, a perfect telluric subtraction. Panels (a) and (b) in Figure 1 show a small cutout of the simulated observations before and after the telluric correction of dataset A. For clarity, an extremely high signal-to-noise of $\text{SNR}_* = 10,000$ is used, with $c = 4 \times 10^{-4}$, making the effects of the different analysis steps visible. Note that the full orbital phase is shown to demonstrate the effect of the waxing and waning of the planet, but for the analysis below only phase angles varying between -45° and $+45^\circ$ around superior conjunction are considered.
3. The data shown in Panel (b) is scaled by its standard deviation in each column, suppressing the parts of the data affected by strong telluric absorption. This is to prevent the cross-correlation signal to be dominated by the more noisy data. Panel (c) in Figure 1 shows the simulated data after this step.

Panel (d) of Figure 1 shows the same as Panel (c), but now for data set B, hence showing only the lines of $^{13}\text{C}^{16}\text{O}$ isotopologue.

3.3. Cross-correlation signal at 2.4 micron

We first demonstrate the use of the cross-correlation technique to detect the $^{13}\text{C}^{16}\text{O}$ isotopologue of carbon monoxide, considering a wavelength range of 2.32 to 2.45 micron, just redward of the wavelength regions probed by several previous observations targeting CO in hot-Jupiter atmospheres (e.g. Brogi et al. 2014). Since these observations only probed out to 2.345 micron, they just missed the bandhead of $^{13}\text{C}^{16}\text{O}$. In Figure 2, we show the opacities of $^{12}\text{C}^{16}\text{O}$ (blue) and $^{13}\text{C}^{16}\text{O}$ (orange) between 2.29 and 2.40 micron. The $^{13}\text{C}^{16}\text{O}$ bandhead at 2.345 micron is clearly visible.

The 100 simulated high-dispersion spectra were each given a signal-to-noise of $\text{SNR}_* = 200$ per wavelength step. First we consider the cross-correlation of data set A (which includes the lines from all molecules and isotopologues) with a pure $^{12}\text{C}^{16}\text{O}$ template spectrum. The latter includes only the $^{12}\text{C}^{16}\text{O}$ opacity in the spectral calculation. This results in a cross-correlation signal with an SNR of ~ 13 (see left panel of Figure 3). This is as expected. The planet/star contrast of this system is 7×10^{-4} ,

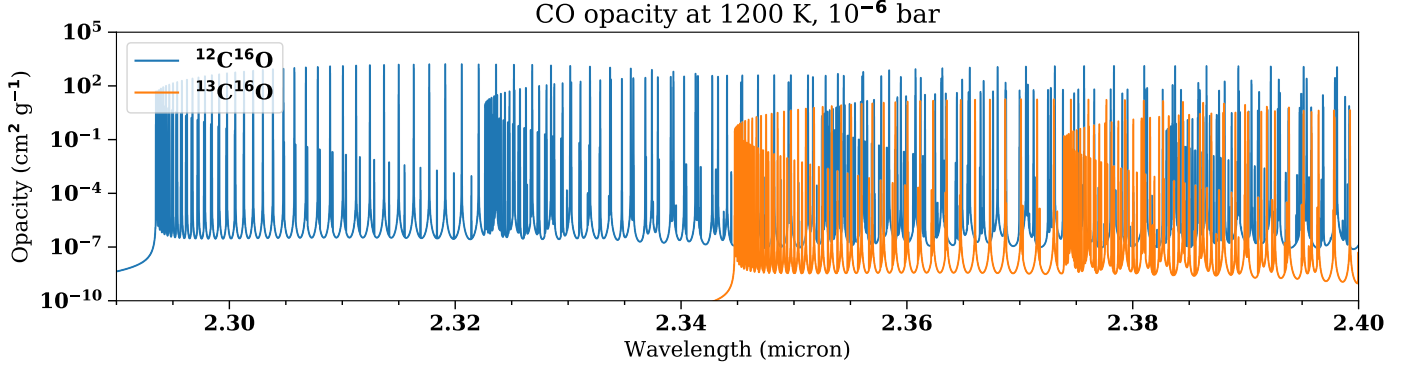


Fig. 2. Opacities of $^{12}\text{C}^{16}\text{O}$ (blue) and $^{13}\text{C}^{16}\text{O}$ (orange), shown at $T = 1200$ K and $P = 10^{-6}$ bar. The opacities have been scaled such that $^{12}\text{C}^{16}\text{O}$ constitutes 98.7 % and $^{13}\text{C}^{16}\text{O}$ 1.1 % of all CO molecules.

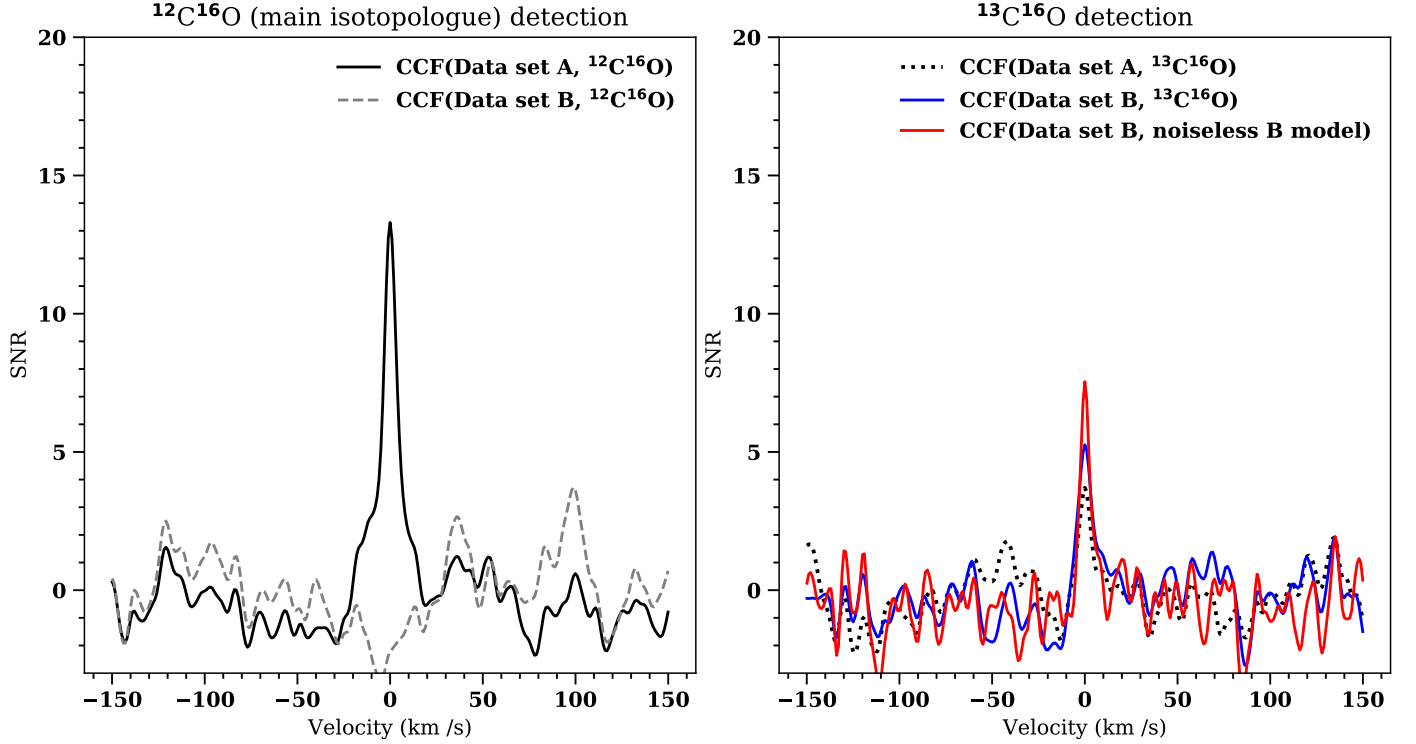


Fig. 3. Results from simulated observations of HD 179949 b consisting of 100 spectra with an SNR_* of 200 each, with a $R=100,000$ spectrograph covering the wavelength range $\lambda = 2.32 - 2.45 \mu\text{m}$. *Left panel:* Cross-correlation function (CCF) using a pure $^{12}\text{C}^{16}\text{O}$ template spectrum on data set A (black solid line) which contains all species, and data set B (grey dashed line) which contains lines of $^{13}\text{C}^{16}\text{O}$ only. Data set A gives a signal with an SNR of ~ 13 , while the main isotopologue, as expected, is not detected in data set B. *Right panel:* CCF using a pure $^{13}\text{C}^{16}\text{O}$ template spectrum on data set A (black dotted line) and data set B (solid blue line). In addition, we show the CCF using a noiseless telluric-free model for data set B as a template (red solid line). The $^{13}\text{C}^{16}\text{O}$ isotope is detected at an SNR of ~ 3.5 and ~ 5 in data set A and B respectively. By using the perfect noiseless input model as a template, $^{13}\text{C}^{16}\text{O}$'s detection SNR is further increased to an SNR of ~ 7 . To reach the latter significance, the planet atmosphere needs to be well constrained.

and the SNR of the combined 100 spectra is 2×10^3 , implying an SNR on the planet spectrum of ~ 1.4 per wavelength step. Note that this is very similar to precisions already reached with existing observations, albeit for a smaller and slightly blueward wavelength region (Brogi et al. 2014). With on the order of 100 strong CO lines in the targeted wavelength region, this combines to an overall SNR of $\sim \sqrt{100} \cdot 1.4 = 14$ (see Appendix A.1 for a derivation), which is in good agreement with the SNR resulting from our more detailed simulations. As a control, we also cross-correlated data set B (from which all spectral lines of the main

isotopologue were removed) in the same way, and naturally no signal was detected (see left panel of Figure 3).

Subsequently, we cross-correlated data set B, i.e. the observation from which all lines of molecules and isotopes other than $^{13}\text{C}^{16}\text{O}$ have been subtracted, with two different models. First, with a pure template spectrum, containing lines only from $^{13}\text{C}^{16}\text{O}$. This is shown in the right panel of Figure 3. $^{13}\text{C}^{16}\text{O}$ is the most abundant of the secondary isotopologues (1.1 % of all CO molecules, see Table E.1), and therefore studied here. This results in a cross-correlation signal with an SNR of ~ 5 . A better matching cross-correlation template is given by the difference between a full planet spectrum model minus the same

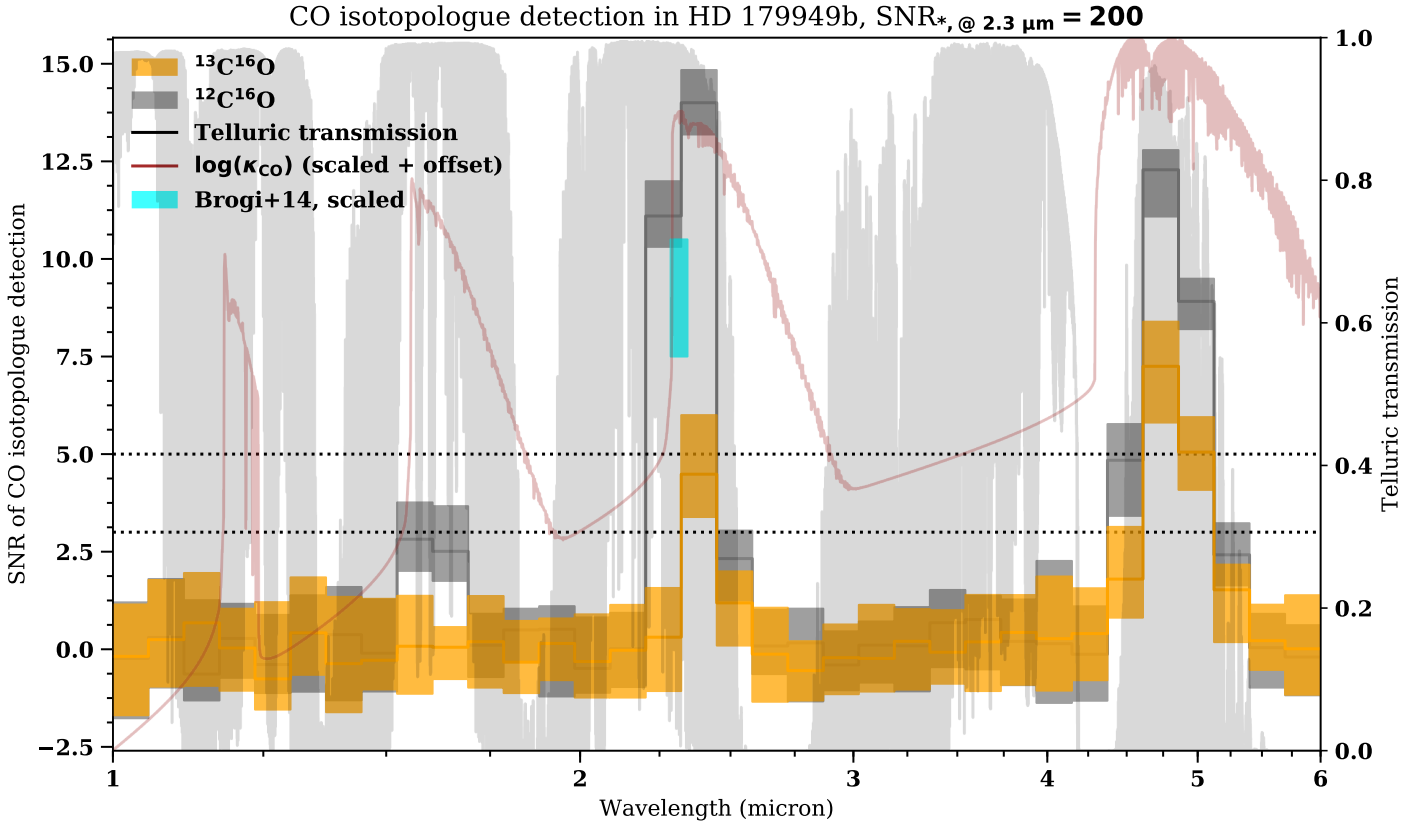


Fig. 4. Wavelength-dependent detection SNR for the secondary $^{13}\text{C}^{16}\text{O}$ (orange boxes) and the main $^{12}\text{C}^{16}\text{O}$ isotopologue (gray boxes). The box widths correspond to the wavelength range of the synthetic observations, while the height corresponds to the 16 and 84 percentiles of the measured SNRs, as derived by running the simulations multiple times. For $^{13}\text{C}^{16}\text{O}$ the SNR of data set B cross-correlated with the pure isotopologue template spectrum are shown, which is conservative, corresponding to the solid blue line in Figure 3. For $^{12}\text{C}^{16}\text{O}$ the SNR of data set A cross-correlated with the pure isotopologue template spectrum are shown. We assumed 100 observations with $\text{SNR}_*(2.3\ \mu\text{m}) = 200$, used to calculate the stellar SNR as function of wavelength. In the background, we show the telluric transmission model (gray solid line), as well as the scaled and offset logarithm of the CO opacity at $T = 1200\ \text{K}$ and $P = 10^{-4}\ \text{bar}$ (light red solid line). The CO detection by Brogi et al. (2014) is shown in cyan. Note that the actual SNR value of the CO detection in Brogi et al. (2014) is 5.8, but due to the larger wavelength coverage of our bins one has to scale this value up to a SNR of 9. This is somewhat lower than our prediction, but the SNR of their observations is also smaller.

constructed without the opacity of $^{13}\text{C}^{16}\text{O}$, a noiseless model B spectrum. This takes potential shielding of $^{13}\text{C}^{16}\text{O}$ lines by the other isotopologues or molecules into account. This results in a cross-correlation signal with an SNR of ~ 7 , and is expected in the case that sufficient spectral information is available such that the planet atmosphere can be well modelled. Even in the worst case, i.e. without removal of the main isotopologue and other molecules from the data (using data set A), the signal from the $^{13}\text{C}^{16}\text{O}$, correlating with the pure $^{13}\text{C}^{16}\text{O}$ template spectrum, is still detected at an SNR of ~ 3.5 , see right panel of Figure 3.

3.4. Wavelength and SNR study

In the previous section we showed that $^{13}\text{C}^{16}\text{O}$ should be readily detectable at 2.4 micron. Here we investigate how such detectability varies as function of wavelength. This is shown in Figure 4, where the expected SNR of $^{13}\text{C}^{16}\text{O}$ (and $^{12}\text{C}^{16}\text{O}$) for the same benchmark hot Jupiter is shown as function of wavelength, for blocks of $\lambda/\Delta\lambda$ of 20, at a resolving power of $R=100,000$, with a wavelength sampling of three pixels, a stellar $\text{SNR}_*(2.3\ \mu\text{m})$ of 200 per step per exposure, and 100 exposures. The stellar SNR at wavelengths different from 2.3 micron was obtained using Equation 4 (using PHOENIX models (Hauschildt

et al. 1999) for the host star, as described in Mollière et al. 2015). It changes from roughly 300 at $1\ \mu\text{m}$ to 80 at $6\ \mu\text{m}$. The grey and orange lines indicate the SNR as function of wavelength for the detection of the $^{12}\text{C}^{16}\text{O}$ and $^{13}\text{C}^{16}\text{O}$ isotopologues, respectively.

For $^{13}\text{C}^{16}\text{O}$ we show the SNR arising from correlating data set B with a pure $^{13}\text{C}^{16}\text{O}$ spectral template, which is conservative, corresponding to the solid blue line in Figure 3. When using the noise-free data set B spectrum as a cross-correlation template, the SNR at, e.g., $4.7\ \mu\text{m}$ would increase from 7 to 10. For the $^{12}\text{C}^{16}\text{O}$ detection we show the SNR arising from correlating data set A with a pure $^{12}\text{C}^{16}\text{O}$ spectral template. The simulations at each wavelength were run multiple times to reduce the stochastic scatter. In Figure 4 the 16 to the 84 percentiles of the SNR distributions are indicated as orange or gray boxes, corresponding to the 1σ uncertainty ranges. The pure isotopologue models were chosen to cross-correlate with the data, to allow direct comparison to the CO detection by Brogi et al. (2014), who used pure (multi-isotopologue) CO models.

For reference, Figure 4 also shows the transmission of the Earth atmosphere (light grey) and the logarithm of the opacity of the carbon monoxide molecule as function of wavelength (light red). As expected, because the isotope-mass differences are small, the main and secondary isotopologue can only be de-

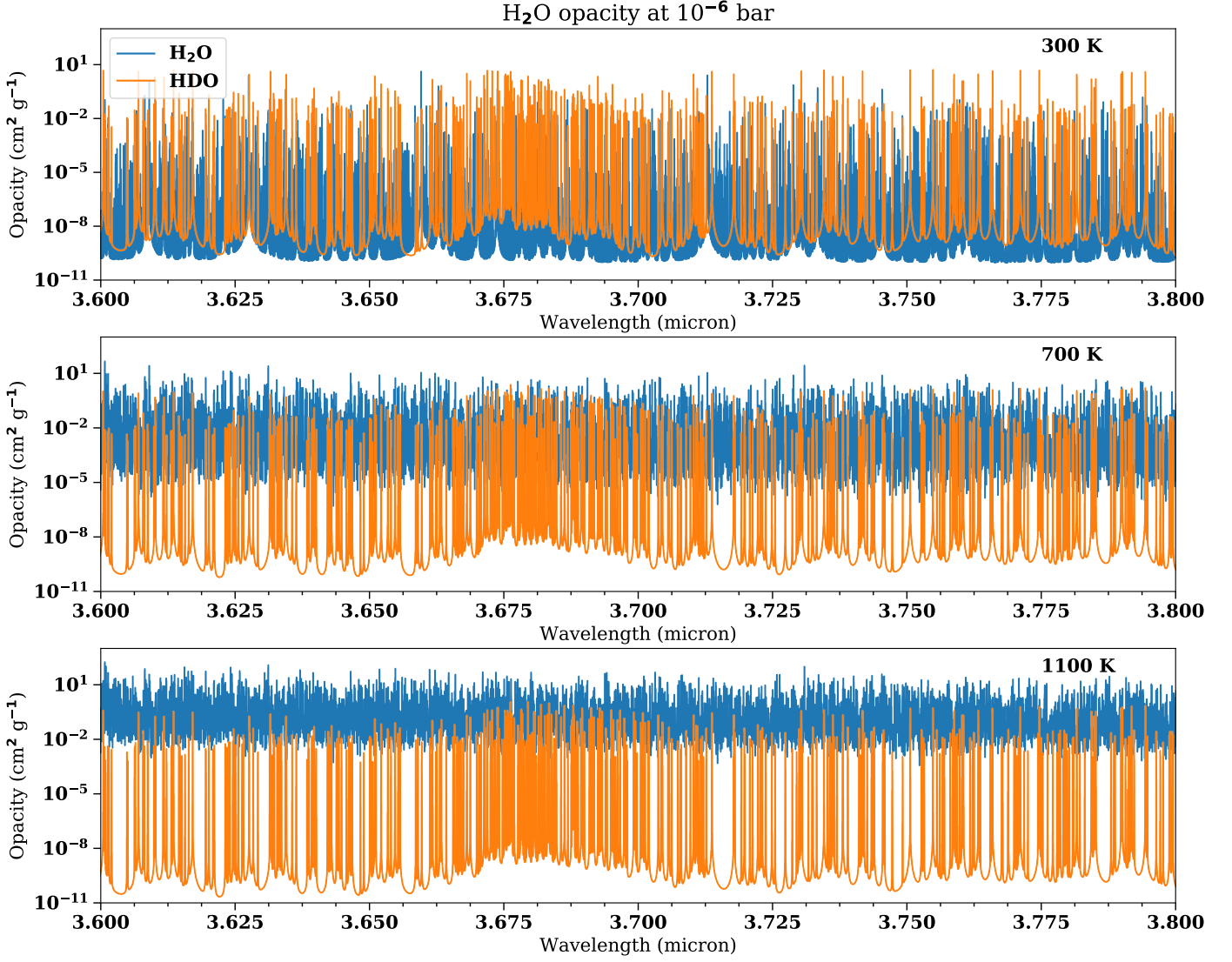


Fig. 5. Opacities of H₂O (blue) and HDO (orange) at $T = 300$ K (*upper panel*), $T = 700$ K (*middle panel*) and $T = 1100$ K (*lower panel*), at $P = 10^{-6}$ bar. The opacities have been scaled such that H₂O constitutes 99.7 % and HDO 4×10^{-5} of all H₂O molecules. The higher the temperature the more shielding of HDO occurs by H₂O.

tected where the CO opacity is high, i.e. at ~ 2.4 micron and around ~ 4.7 micron. Because our simulation includes the stellar photon noise variations as a function of wavelength, we see that the latter (4.7 micron) is more efficient for the $^{13}\text{C}^{16}\text{O}$ detection, with an expected SNR of 7 for the assumptions given above. Note that we ignored the telluric thermal background in our calculations, hence this may be different for fainter targets.

Figure 4 also shows the literature SNR of the CO detection in the 2.3 micron region, as reported by Brogi et al. (2014). Their SNR value (5.8) was scaled up to 9 to account for the fact that our wavelength bins are broader. Their detection SNR is broadly consistent at roughly 80% of the prediction presented here, resulting from data with overall a somewhat lower signal to noise. Hence we expect $^{13}\text{C}^{16}\text{O}$ to be detectable with *CRILES+* on the VLT.

4. Detecting HDO in atmospheres of self-luminous planets

Here we focus on the detectability of HDO in the thermal spectra of young, self-luminous gas-dominated planets. In the light

of planet formation and evolution, a planet's D/H ratio is arguably the most interesting isotope ratio to study. Both atmospheric evaporation and icy planetesimal accretion can have a noticeable impact, both tending to increase the atmospheric D/H ratio. In contrast, substellar objects more massive than $13 M_{\text{J}}$ can burn their deuterium, regardless of their formation pathway (Saumon et al. 1996; Chabrier & Baraffe 2000; Burrows et al. 2001; Baraffe et al. 2003; Mollière & Mordasini 2012; Bodenheimer et al. 2013), and observations of deuterium in these objects has been suggested as a test for whether their mass is above or below the deuterium burning threshold (Béjar et al. 1999; Pavlenko et al. 2008).

The main wavelength region of interest for HDO measurements is around 3.7 micron, where at low temperatures ($T \lesssim 600$ K), and for galactic abundances ($\text{HDO}/\text{H}_2\text{O} \approx 4 \times 10^{-5}$) the HDO opacity protrudes through a minimum of the opacity of the main isotopologue of H₂O. For example, this wavelength region has been used to study the HDO abundances on Mars, (see, e.g., Villanueva et al. 2015). The detectability of HDO at a given D/H ratio is expected to strongly depend on atmospheric temperature. While it is obvious that thermal emission from cool

planets is more difficult to detect than that from warm planets, the 3.7 micron region is, in contrast, relatively clean from H₂O opacity at low temperature, but largely blanketed by it in hotter atmospheres. This is shown in Figure 5, where the water opacities in the 3.7 micron region are plotted relative to those of HDO for different temperatures.³ We therefore expect that HDO will be best detected in relatively cool, directly imaged planets, such that the angular separation from their host star leads to a much decreased stellar flux and noise in the planet spectrum.

Unfortunately, HDO measurements may be hampered by blanketing by CH₄ absorption in the same wavelength range. However, the latter may be quenched, meaning that methane poor gas is mixed up from deeper hotter regions in the atmosphere. This particular case is therefore also studied below (see Section 4.4). Note that we investigate the detectability of CH₃D in Section 5.

4.1. Synthetic observations

The atmospheric structures were calculated using the *petit-CODE* as introduced in Section 2.1, for which we assumed self-luminous planets, with a surface gravity of $\log_{10}(g) = 3.5$ (cgs), a solar composition ($[\text{Fe}/\text{H}] = 0$), and the temperature varying from 300 to 1500 K in $\Delta T = 100$ K steps. Clouds were neglected in the calculations. These are models modified from the atmosphere grid calculated for Samland et al. (2017), where *HITRAN* opacities are used for NH₃ and PH₃ in the structure calculations. Note that here we use their *Exomol* counterparts for the high-resolution calculations.

Since non-equilibrium chemistry can quench the CO, CH₄ and H₂O abundances in lower-temperature planets, by mixing up CO-rich and CH₄-poor material from high-temperature, high-pressure regions of the planets (see, e.g., Zahnle & Marley 2014), we consider models both with equilibrium abundances, as well as models where CH₄ (and CO₂) has been excluded in the chemical equilibrium calculations, constituting an extreme quenching scenario (see Section 4.4). The exclusion of CO₂ was necessary because equilibrium chemistry would otherwise lock up oxygen in this molecule, which should stay in H₂O in the real quenching case. We also found that the carbon in CO is preferentially moving into C₂H₂ at low pressures and temperatures ($T \lesssim 140$ K), but CO does not have any features in the 3.7 micron region, so this effect was neglected here.

Subsequently, high-resolution spectra for the planets were calculated as described in Section 2.2, taking into account the opacities of H₂O, CO, H₂S, NH₃, PH₃, CH₄ and CO₂, as well as H₂-H₂ and H₂-He CIA. Nominally, the HDO/H₂O ratio was assumed to be twice the cosmic D/H ratio 2×10^{-5} . The factor 2 arises from combinatorics, i.e. the fact that every water molecule has two locations where D may be placed, instead of H, when forming HDO instead of forming H₂O (note this is a factor 4 for CH₃D). The wavelength region considered here was from 3.6 to 3.8 micron. As before, we assumed a resolution of 10^5 , and three wavelength steps per resolution element.

³ Note that we use *HITEMP* water opacities, for which the secondary isotopologue lines are taken from the *HITRAN* line list. *HITRAN* is known to be incomplete at high temperatures, but also the high-temperature *Exomol* line lists both for H₂O (Barber et al. 2006) and HDO (Voronin et al. 2010) exhibit this behaviour when inspected with the *Exomol* cross-section service (Hill et al. 2013).

4.2. Analysis of the synthetic observations

The analysis of the synthetic observations is similar to that for CO described in Section 3.2. The main difference is that the planet does not exhibit any measurable change in its radial velocity offset during the observations (assuming a long >year orbital period). Therefore, it is not the change in Doppler shift that is used to separate the planet spectral features from that of the star and the Earth atmosphere. Instead, both the planet and star are observed simultaneously, but angularly separated, allowing the stellar spectrum to be used for removing the stellar and telluric contributions from the planet spectrum (Snellen et al. 2015).

Template planet spectra $F_P(\lambda)$ and $F_{P-\text{HDO}}(\lambda)$ are created, which are identical except that the latter has its HDO opacity removed. Comparing to Section 3.2, $F_P(\lambda)$ corresponds to template spectrum A (without tellurics and noise) and $F_P(\lambda) - F_{P-\text{HDO}}(\lambda)$ to template spectrum B. In principle, subsequent analysis would involve the addition of noise and telluric absorption, followed by reduction steps similar as for the hot Jupiter case described in Section 2.3. However, since this procedure must be performed many times, we derived, tested, and used the following equation to approximate the statistical detection level of HDO for an observation with a certain SNR per wavelength step:

$$S/N = \frac{1}{\sigma} \left\{ \sum_{i=1}^{N_\lambda} [F_P(\lambda_i) - F_{P-\text{HDO}}(\lambda_i)]^2 \right\}^{1/2} \\ = \frac{1}{\langle F_P \rangle} (S/N)_{\text{pix}} \left\{ \sum_{i=1}^{N_\lambda} [F_P(\lambda_i) - F_{P-\text{HDO}}(\lambda_i)]^2 \right\}^{1/2}, \quad (5)$$

where σ is the error in the spectrum per wavelength step, N_λ is the number of spectral points, $(S/N)_{\text{pix}}$ is the average SNR per wavelength step, and $\langle F_P \rangle$ is the average flux per wavelength step in the targeted spectrum. The derivation of Equation 5 is given in Appendix A.2. This approximative formula predicts the SNR of the HDO detection when cross-correlating data set B with the noiseless B model (corresponding to the red solid line in the right panel of Figure 3).

This formula was tested by comparing it to the full synthetic analysis (i.e. adding tellurics and noise, reducing the data, cross-correlating with an HDO template), leading to a good agreement, see Appendix B.1. The reader should note that due to the complexity of the HDO spectrum, and methane absorption that causes a quasi-continuum depending on the atmospheric temperature, even simpler SNR estimates as mentioned for CO in Section 3.3 (SNR scaling with $N_{\text{lines}}^{1/2}$, where N_{lines} is the number of lines) are not adequate.

4.3. Required spectral SNR to detect HDO

In Figure 6 we show the required SNR per pixel of a planet spectrum for detecting HDO at a SNR of 5, in the 3.6 to 3.8 μm region, as a function of planetary T_{equ} and D/H ratio. These were calculated using Equation 5.

The required SNR per pixel increases as function of temperature, e.g. for the cosmic D/H ratio from ~ 1 at 400 K to ~ 10 at 1200 K, due to the increased shielding by H₂O absorption at higher temperatures. The 3.7 μm region is relative clear of water absorption at low temperatures. The reader should note, however, that it is generally more difficult to reach a certain SNR level for a cooler planet than for a warmer planet. The required SNR per pixel flattens out at higher temperatures due to the ex-

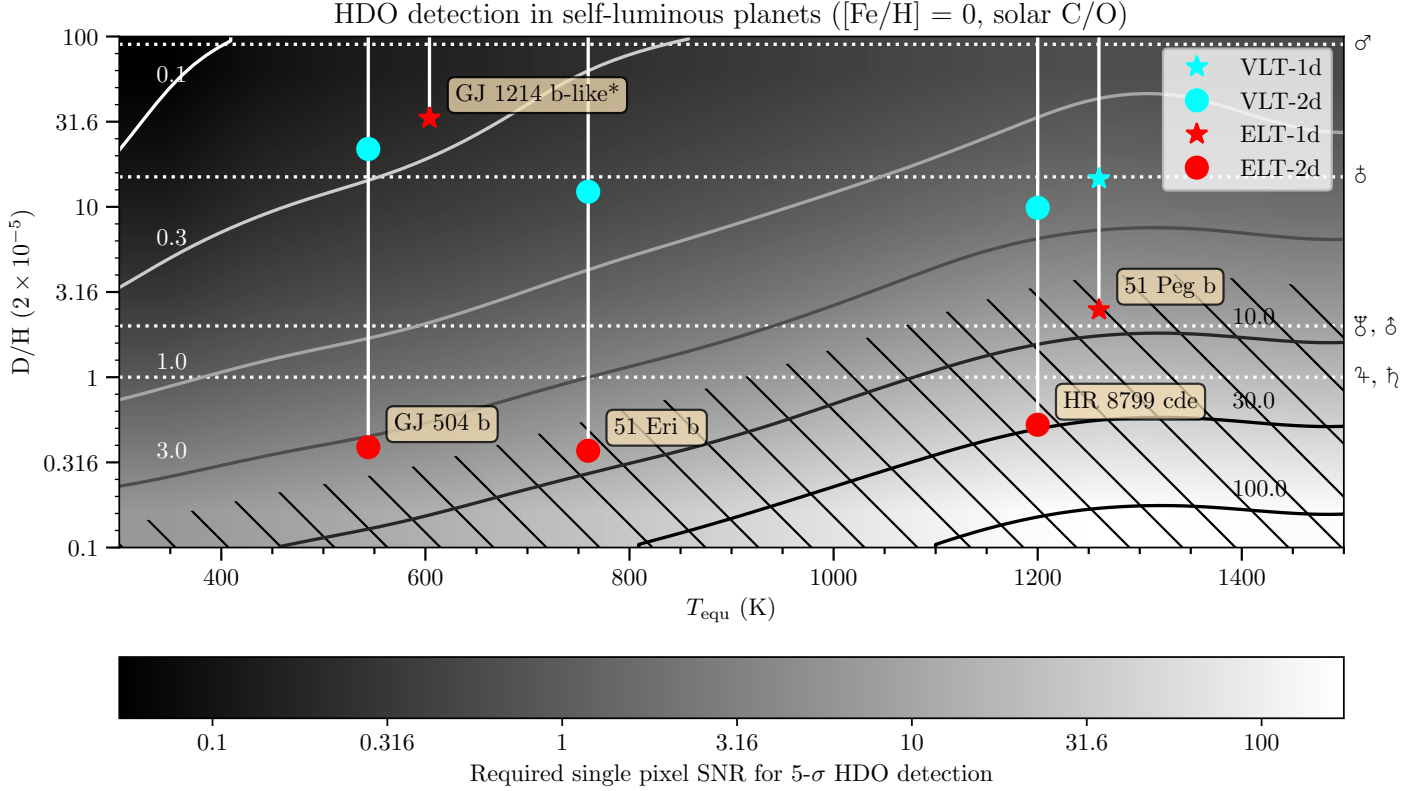


Fig. 6. Contour map showing the required SNR of the planetary spectrum per pixel, as function of planetary temperature and D/H ratio, for an HDO detection at an SNR of 5. The considered wavelength region is 3.6 to 3.8 micron. The D/H ratios of the Solar System planets are indicated by the horizontal white dotted lines. The colored symbols indicate the lowest detectable D/H ratios for various exoplanets. Cyan and red symbols indicate limits for *CRILES+*@VLT and *METIS*@ELT, respectively, assuming a single night of observation (10 h). Filled circles stand for those targets which can be angularly separated from their host star, assuming a stellar flux reduction at the planet position by a factor 100 and 1000 for the VLT and ELT, respectively. Star-symbols denote planets that cannot be spatially resolved, e.g. hot Jupiters, hence no flux suppression is possible. *Note that *GJ 1214 b-like* planet is a hypothetical non-transiting twin of GJ 1214 b at half the distance from Earth. The hatched area indicates the region where the required SNR per pixel is larger than 5, implying very weak planet lines, which may be difficult to recover with planet atmospheric modeling.

pected decrease in methane abundance. Obviously, HDO is easier to detect if the atmospheric D/H ratio is higher. At 400 K, only an SNR per pixel of 0.1 is needed if the D/H ratio is 100 times the cosmic value (e.g. that of Mars).

It is instructive to compare the results presented in Figure 6 with the expected SNR limits of known exoplanets achievable with the current 10m-class telescopes and the future Extremely Large Telescopes (ELTs). For this we concentrate on the *CRILES+* instrument (Follert et al. 2014) on ESO’s VLT (cyan symbols) and *METIS* (Brandl et al. 2014) (red symbols) on the European ELT, and a few prototypical exoplanets indicated in Figure 6, assuming a single night (10 hr) of observations. The planetary parameters used for this study are given in Table F.1.

For *CRILES+* on the VLT, we assumed an instrument resolution of $R = 100,000$, three pixels per resolution element, a mirror surface area of 52 m², and a total telescope+instrument throughput of 0.15. For *METIS* on the ELT, identical specifications were assumed, but the mirror surface area was changed to 976 m². The planetary flux was estimated by interpolating our synthetic, self-luminous exoplanet models to the planets’ published equilibrium temperature, and subsequently using the planet radius and distance to the Solar System to scale the flux accordingly. The effect of the planetary log(*g*), composition, and cloudiness are hence neglected in the SNR estimates pre-

sented here. The stellar flux was obtained in the same way, using *PHOENIX* models (Hauschildt et al. 1999) for the host star spectra, as described in Mollière et al. (2015). Finally, the expected SNR per pixel for one night of observations was obtained by computing the mean number of photons per instrument pixel of both planet and star, and then calculating

$$(S/N)_{\text{pix}} = \frac{N_p}{(N_p + N_*/f)^{1/2}}, \quad (6)$$

where N_p and N_* are the number of photons per pixel of planet and star, respectively. The factor f denotes the amount of starlight reduction at the planet position. In the case that planet and star are not angularly separated, denoted as VLT-1d and ELT-1d, there is no starlight reduction and $f = 1$. For directly imaged planets, denoted as VLT-2d and ELT-2d in Figure 6, f is assumed to be 100 and 1000 for VLT-2d and ELT-2d observations respectively, using slit-spectroscopy, or the integral field unit in the case of *METIS* (e.g. Snellen et al. 2015).

The reader should note that we do not take the sky background into account for these calculations, which is typically at 7.5–8 mag arcsec⁻² at these wavelengths. At the angular resolution of the VLT and ELT, taking into account the stellar flux reduction at the planet position of 100 and 1000 respectively, the sky background becomes relevant for stars fainter than $m_L \sim 6$

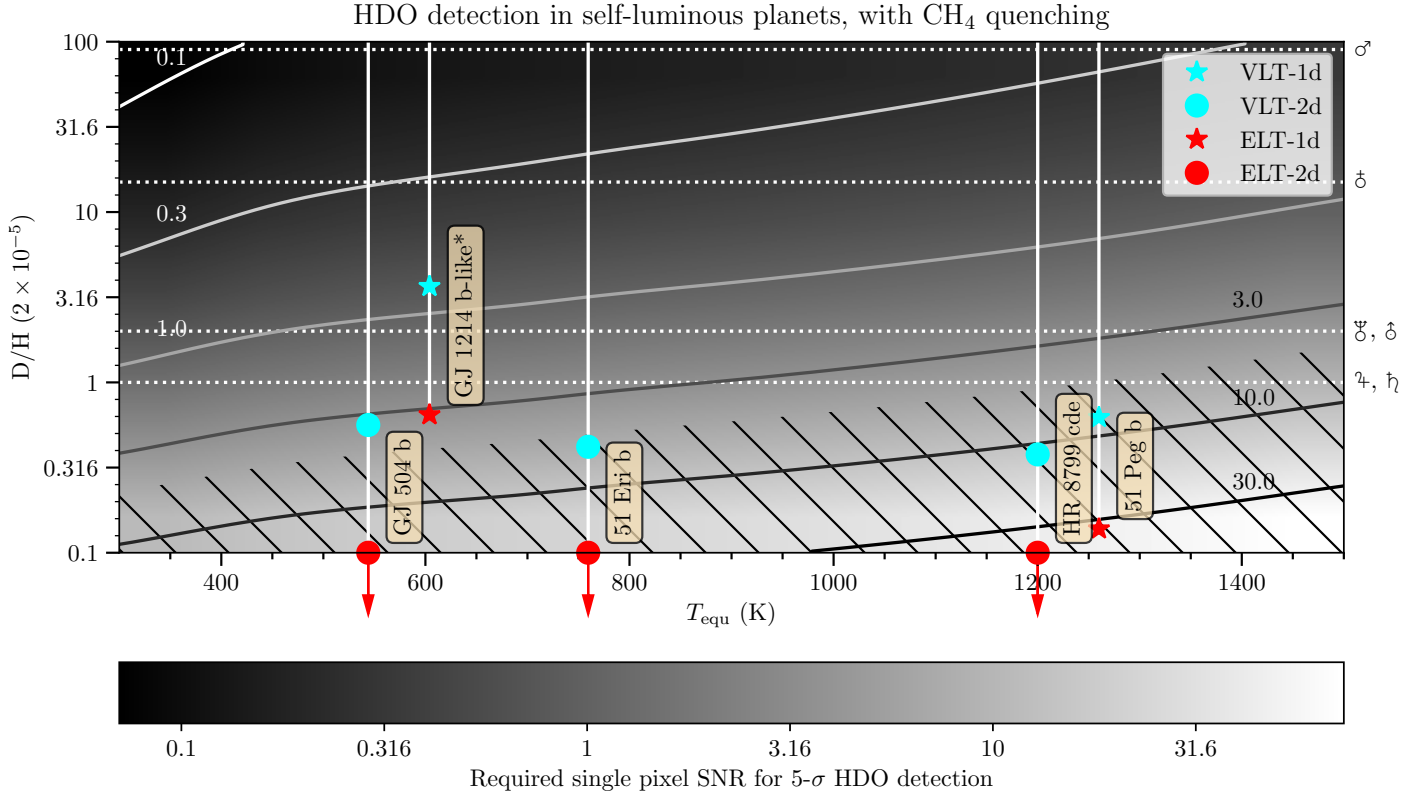


Fig. 7. Same as Figure 6, but neglecting both CH_4 (and CO_2) in the chemistry and for the opacities, in order to mimic an atmosphere where CH_4 , CO , and H_2O are quenched at high pressures (i.e. high temperatures).

for the VLT and $m_L \sim 7$ for the ELT in our simulations. For brighter stars, the residual starlight will dominate over the sky background at the planet position.

Individual planets:

GJ 504b, 51 Eri b, HR 8799 cde

For the directly imaged planets GJ 504b, 51 Eri b, and HR 8799 cde, assuming equilibrium chemistry, we expect that galactic D/H ratios will be out of reach for 10m class telescopes. With the ELT, galactic D/H ratios are all in reach within a single night.

Super Earths: GJ 1214b-like planets

GJ 1214 b (and other planets like it) is an interesting target since it is of low mass ($6.5 M_\oplus$ Charbonneau et al. 2009), significantly irradiated ($T_{\text{equ}} \sim 600$ K, see Table F.1), and potentially highly enriched in icy planetesimals and therefore could have a high D/H ratio. Note that it is not expected that recently formed, self-luminous planets of this mass would ever exhibit such temperature, due to the low amount of formation heat retained (Linder et al., submitted). While GJ 1214 b itself is too faint, similar non-transiting systems should be found at smaller distances. With a transit probability of $\sim 7\%$, the nearest non-transiting GJ 1214 b-like system is expected to be found at approximately half the distance, with a host star 2 magnitudes brighter, which we used for our simulations.

Using *METIS* on the ELT, we expect that atmospheric D/H ratios ≥ 30 times the galactic mean value may allow for the detection of HDO in a single night. Current theories point to GJ 1214 b being strongly enriched in metals (by a factor 100 to

1000 w.r.t. solar, see Morley et al. 2013, 2015; Mollière et al. 2017), a large D/H ratio may well be expected for this type of planet (see the discussion in Section 1), although probably not as high as 30. Note that we assume solar abundances in the spectral models used here, so only D/H varies. Moreover, the spectral models used here were for self-luminous planets, while the GJ 1214 b-twin planet is irradiated.

51 Peg b

Similar to the GJ 1214b-like case studied above, we use our self-luminous atmospheric grid to study the detectability of HDO in the atmosphere of the hot Jupiter 51 Peg b. While this planet is not a self-luminous planet, our analysis gives a first estimate of the single-pixel SNR to be expected for hot Jupiters. Here we predict that one night of observations with VLT *CRISP*+ will allow to detect HDO if the atmospheric D/H ratio is 10 times the galactic value or higher, while ELT *METIS* would allow detecting HDO down to D/H ratios of twice the galactic value. For a gas giant like 51 Peg b one would expect a D/H ratio similar to the galactic value (see Section 1), which could be reached in four nights with ELT *METIS*, thus remaining a challenge.

It is important to note that, for the hotter planets, large SNRs per pixel are required to detect HDO. For HR 8799 cde and 51 Peg b, the required SNR per pixel is >10 for the detection of HDO at galactic D/H values, implying intrinsically very weak HDO lines. This requires very accurate and complete planet atmospheric modeling, since all weak planet lines need to be accounted for at this level. This is something which has to be investigated in future studies. The region where the required SNR per pixel is larger than 5 is hence indicated by the hatched area in Figure 6.

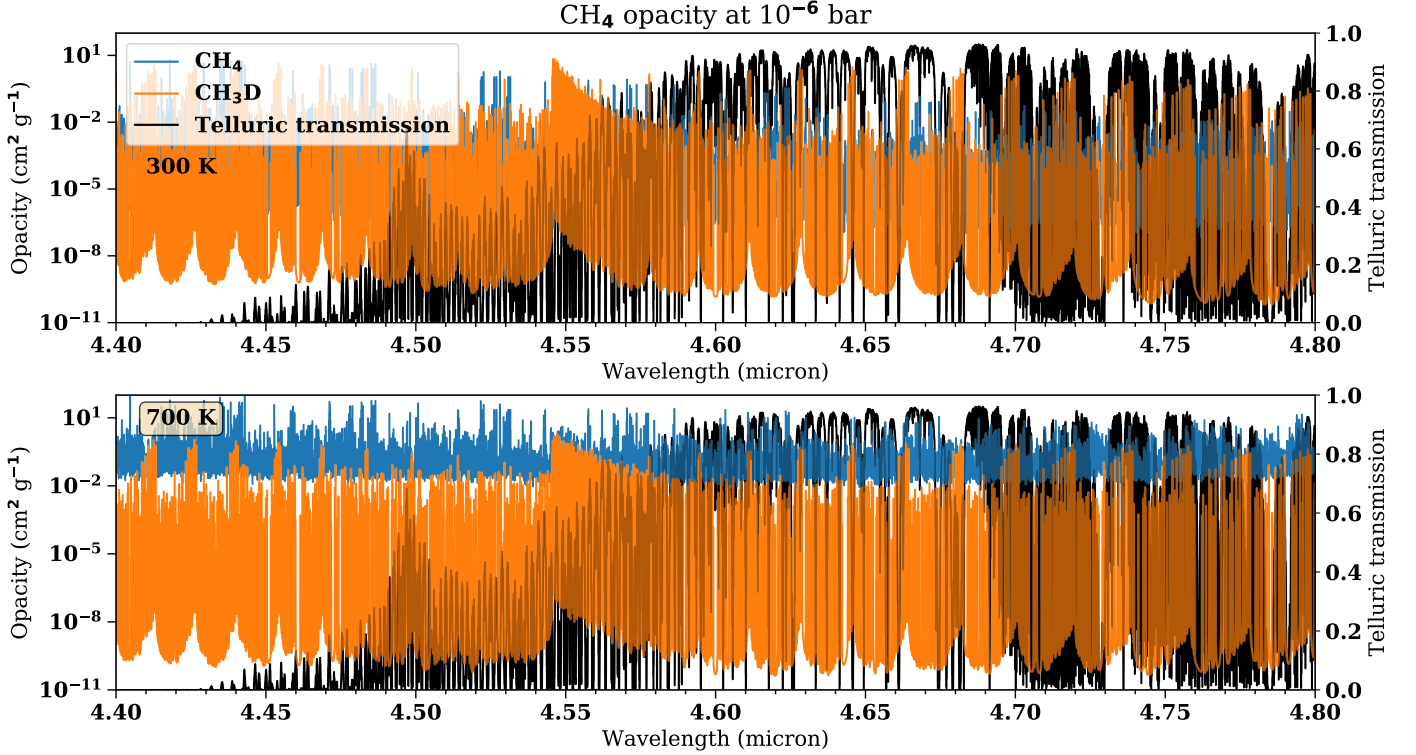


Fig. 8. Opacities of CH_4 (blue) and CH_3D (orange), shown at $T = 300\text{ K}$ (upper panel) and $T = 700\text{ K}$ (lower panel), at $P = 10^{-6}\text{ bar}$. The opacities have been scaled such that CH_4 and CH_3D constitute 98.8 % and 8×10^{-5} of all CH_4 isotopologues, respectively. The telluric transmission is shown in black.

4.4. HDO detection with methane quenching

The results for the methane-depleted calculations (see Section 4.1) are shown in Figure 7. As expected, the required single-pixel SNR to detect HDO decreases substantially: HDO at galactic abundances can now be detected in a single night of VLT *CRIRES+* observations in all example planets, except for the GJ 1214 b-like case. The required SNR per pixel for these cases is lower than 5 out to 1200 K, implying significantly stronger HDO lines than in the default non-quenching case. The gain in sensitivity is due to the fact that methane is not blanketing the HDO lines, but also because we effectively peer into the deeper, warmer and therefore brighter regions of the planet atmosphere.

Moreover, the required SNR in the quenching case is a monotonously increasing function of T_{equ} for all D/H ratios. The plateau seen in the non-quenching case is not present and therefore evidently caused by the decrease in methane absorption with temperature.

5. Detecting CH_3D in self-luminous planets

In this section, we study the detectability of the methane isotopologue CH_3D , which has been used to infer the D/H ratio in Uranus, Neptune, Saturn, and Jupiter, and in the atmosphere of Saturn’s moon Titan (see, e.g., de Bergh 1995; Owen & Encrenaz 2003).

Here we focus on the rovibrational CH_3D band centered around 4.6 micron. This band has the advantage that both the expected planet CH_4 and H_2O opacity are comparatively low, making this wavelength range ideal for the detection of CH_3D . Consequently, this wavelength region has been recently advertised for detecting CH_3D in WISE 0855 (Morley et al. 2018; Skemer et al. 2016). This is also visible in Figure 8, which

shows the opacities of CH_3D and CH_4 at temperatures of 300 and 700 K, and the telluric transmission in the 4.6 micron region.

Similar to the behaviour seen for HDO and H_2O (see Figure 5 and the discussion in Section 4), CH_3D is weaker with respect to CH_4 at higher temperatures, because the lines in the opacity minimum of CH_4 are stronger at high temperature and blanket the CH_3D opacity. We use the *HITRAN* line list for CH_3D , and *Exomol* for CH_4 . Because the telluric absorption is relatively strong shortward of 4.6 micron, our analysis concentrates on the range between 4.6 and 4.8 micron. Future analyses may include the relatively strong CH_3D feature at 4.55 micron requiring highly accurate telluric corrections.

In terms of opacity and chemical abundances, we expect CH_3D to be most easily detected in cool exoplanets, where CH_3D is sufficiently strong compared to CH_4 , and equilibrium chemistry predicts high methane abundances for H_2/He dominated atmospheres. Hotter planets are expected to have a lower methane abundance both due to chemical equilibrium effects and methane quenching (see, e.g. Zahnle & Marley 2014), as discussed earlier.

5.1. Synthetic observations and analysis

The same atmospheric models of self-luminous gas giant planets were used as for the HDO study, focussing on the wavelength range from 4.6 to 4.8 micron, and assuming a CH_3D abundance of 8×10^{-5} , relative to CH_4 .⁴ All nominal isotopologue abundances used in this paper can be found in Table E.1.

⁴ The 4-fold increase when compared to the galactic mean value (2×10^{-5}) is again caused by combinatoric effects.

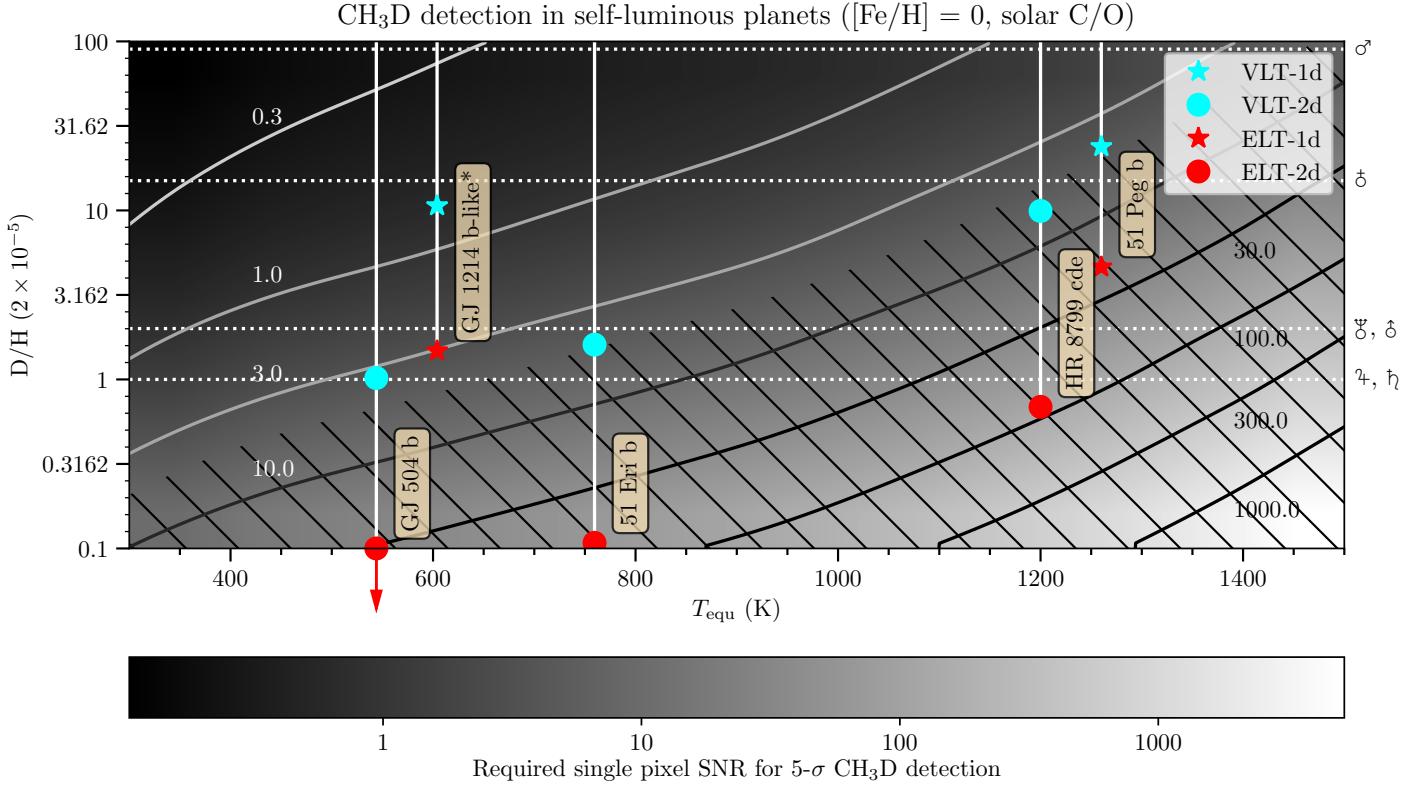


Fig. 9. Same as Figure 6, but for CH₃D.

We use the same analysis technique as described in Section 4.2. However, Equation 5 was modified, since this wavelength region is more strongly affected by telluric absorption. The derivation follows the same principles outlined in Appendix A.2, but accounts for the attenuation by tellurics, leading to scaling of the flux with \mathcal{T} , and of the photon noise with $\mathcal{T}^{1/2}$, where \mathcal{T} is the telluric transmission:

$$S = \sum_{i=1}^{N_i} \mathcal{T}(\lambda_i) [F_P(\lambda_i) - F_{P-HDO}(\lambda_i)]^2, \quad (7)$$

$$N = \left\{ \sum_{i=1}^{N_i} [F_P(\lambda_i) - F_{P-HDO}(\lambda_i)]^2 \sigma_{\text{telluric}}^2(\lambda_i) \right\}^{1/2}, \quad (8)$$

where the effective single-pixel noise is defined by $\sigma_{\text{telluric}} = \mathcal{T}^{1/2} \sigma_{\text{clear}}$, with σ_{clear} being the noise for a fully transparent Earth atmosphere. The SNR of the CH₃D detection is subsequently given by the ratio of equations 7 and 8.

Analogous to the HDO detection case, this approximation was tested by comparing to the full synthetic analysis (i.e. adding tellurics and noise, reducing the data, cross-correlating with an CH₃D template), again leading to good agreement, see Appendix C.

5.2. Required SNR to detect CH₃D

In Figure 9 we show the required SNR per pixel of planetary spectra to detect CH₃D at an SNR of 5, as a function of D/H and planetary equilibrium temperature, in the 4.6 to 4.8 micron region. Analogous to the HDO study in Section 4, we overplot the expected SNRs for known planetary systems, assuming a single night (10 hr) of observations for the VLT and ELT.

For the cooler planets ($T_{\text{equ}} < 800$ K), CH₃D may be detectable using *CRIRES+* on the VLT, except for the GJ 1214 b-twin. Hence, we expect CH₃D may be easier to detect than HDO, and therefore could be preferable for determining the D/H ratio in cool planetary atmospheres (cf. Figure 6). However, in the case of strong methane quenching (cf. Figure 7), HDO is more easily detected than CH₃D, even easier than CH₃D in a non-quenched planet atmosphere.

For the hotter planets, ($T_{\text{equ}} > 1000$ K), we expect that under equilibrium chemistry conditions, HDO is better suited than CH₃D for inferring D/H, even though the retrievable D/H ratios at fixed planetary temperature are comparable in both the CH₃D and HDO case. This is because the required SNR on the planetary spectrum are a factor of 3 larger in the CH₃D case, again raising the question if models can actually predict the planetary flux accurately enough at such a high precision.

We hence expect that CH₃D is the favorable isotopologue when trying to infer D/H ratios in planets cool enough that quenching can be neglected. However, the required SNR per pixel will be larger than 5 for temperatures > 600 K, because the CH₄ opacity is stronger than that of CH₃D at such temperatures. Furthermore, the abundance of all methane isotopologues (also the main isotopologue CH₄) are expected to be lower at high temperatures, making the detectability of CH₃D even more difficult. If quenching is strong, HDO represents the better choice at all temperatures.

6. Detecting HDO in Proxima Centauri b

Proxima Centauri b is a recently discovered planet in the habitable zone of the Sun's closest stellar neighbor (Anglada-Escudé et al. 2016). With $M_{\text{min}} = 1.27 M_{\oplus}$, only slightly more massive than the Earth, it has likely a mainly rocky composition with a climate allowing possibly liquid water on its surface (Ribas et al.

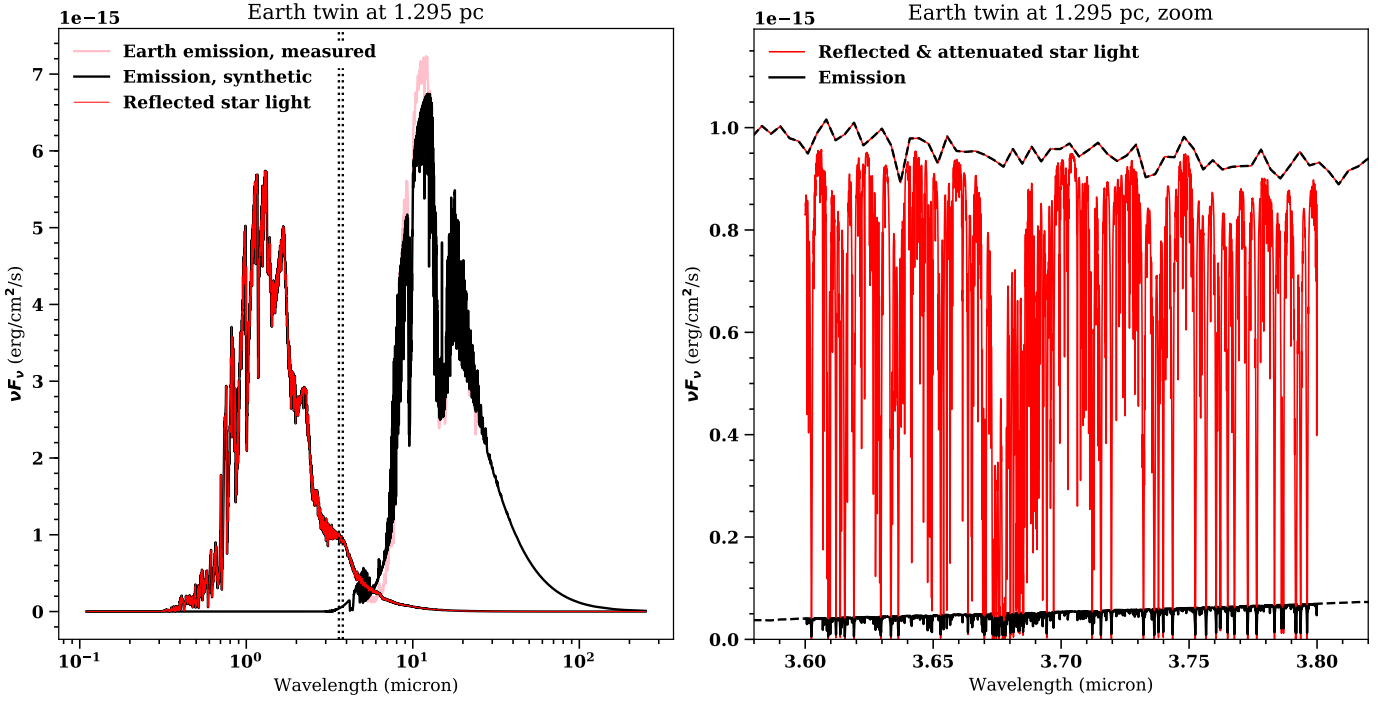


Fig. 10. Apparent spectrum of Proxima Cen b at a distance of 1.29 pc, assuming it is identical to Earth. *Left panel:* The planet synthetic thermal spectrum, assuming the Earth’s P - T profile and abundances is shown as a black solid line. As a comparison, measurements by the *Nimbus 4* satellite are shown as a pink solid line, which largely overlap. The red solid line shows the reflected light assuming a surface albedo of 30 %, neglecting the effect of the planet’s atmosphere. The two vertical black dashed lines denote the wavelength region of interest for probing HDO (3.6 to 3.8 μm). *Right panel:* The same but focused on the 3.6 to 3.8 μm region. The reflected starlight spectrum (red) now includes also attenuation by the planet atmosphere. The colored dashed line shows its unattenuated, low-resolution counter-part from the left panel. At these wavelength, the reflected starlight is ~ 15 times stronger than the intrinsic thermal emission from the planet.

2016; Turbet et al. 2016). In this section, we investigate whether HDO could be detected in the spectrum of Proxima Cen b, assuming atmospheric properties identical to that of Earth.

The properties of the planet atmosphere remain yet unknown. However, extreme irradiation conditions and (partial) atmospheric loss likely play or have played an important role on this planet: models estimate stellar wind pressures multiple orders of magnitudes higher than experienced by Earth (Garraffo et al. 2016). In addition, stellar X-ray and EUV fluxes could have caused loss of water by evaporating Proxima Cen b’s atmosphere, especially when its host star was still in the pre-main-sequence phase. The total loss of water was likely less than an Earth’s ocean, however (Ribas et al. 2016).

If Proxima b has retained sufficient water, partly in liquid form on its surface, life could possibly have formed and developed. However, any lifeforms that Proxima Cen b was or is hypothetically harboring may have had to develop a UV tolerance much higher than organisms with even the highest UV tolerance on Earth (e.g. *Deinococcus radiodurans*). Assuming an Earth-like atmosphere, the recently observed super-flare from its host star and its derived flare rate spectrum suggests that no ozone could survive in the atmosphere of Proxima b, ending all hypothetical life on Proxima Cen b with a single super flare (Howard et al. 2018).

It is unclear what types of climate the planet’s orbit and assumed tidally-locked or resonating spin rate allow, which also depends on the atmospheric composition. This has, e.g., been studied in Turbet et al. (2016), with as main conclusion that conditions on the planet may allow for the existence of liquid water on its surface, for example on the dayside for a tidally locked

case, with an 1 bar N_2 and slightly enriched in CO_2 w.r.t. Earth, or all along the equator in the case of a 3:2 resonance between spin and orbital motion (with 1 bar N_2 and enriched in CO_2).

With Proxima Cen b’s actual atmospheric state unknown, we study the case of an Earth-twin in emitted and reflected light assuming a circular orbit with a radius of 0.0485 AU (Anglada-Escudé et al. 2016). For modeling the planet spectrum, we used the P - T structure of Earth as shown in Figure 1.3 in Bigg (2004). Motivated by the values in Table 1.1 in Bigg (2004), we chose very simple abundance models for the planet atmosphere: for water, a uniform volume mixing ratio of 0.5 % within the troposphere ($P > 0.3$ bar); for ozone 0.7 ppm within the stratosphere ($P < 0.3$ bar), and for CO_2 and CH_4 , vertically homogeneous volume mixing ratios of 400 (including alien fossil fuel emission) and 1.75 ppm, respectively. We assumed the a D/H value of 2×10^{-4} , similar to that of Earth.

In the left panel of Figure 10 the resulting low-resolution ($\lambda/\Delta\lambda = 1000$) synthetic emission spectrum (black solid line) is plotted over the observed average Earth emission spectrum (pink solid line) as measured by the *Nimbus 4* satellite between 6.25 and 25 μm (Hanel et al. 1972). The agreement is close enough for the study presented here. The synthetic spectrum has been obtained with *petitCODE* (Mollière et al. 2015, 2017). The reflected light spectrum is shown in red, assuming an airless planet with a surface albedo of 30 %. A Proxima Cen-like stellar spectrum was taken from *PHOENIX* models (Hauschildt et al. 1999). We assumed an effective temperature and radius of 3042 K (Ségransan et al. 2003) and $0.1542 R_\odot$ (Kervella et al. 2017).

For the high resolution study in emitted light we calculate the spectrum in the same way as in the low resolution case above, this time using our high resolution code described in Section 2.2. For the reflected light case, the only atmospheric process we consider is attenuation of the stellar light due to scattering and absorption. Atmospheric emission and scattering into the ray that is propagating through the atmosphere is neglected. Hence, we assume that the stellar flux is reflected at the Earth's surface, and attenuated on its way to and from the surface. In this case, the reflected flux measured by an observer at distance d from a planet, when viewing its dayside, is

$$F_{\text{refl}}(\lambda) = 2A(\lambda)F_*(\lambda)\left(\frac{R_p}{d}\right)^2 \int_0^1 \mu^2 e^{-2\tau(\lambda)/\mu} d\mu, \quad (9)$$

where A is the surface albedo of the planet (assuming isotropic scattering), F_* is the stellar flux measured at the substellar point of the planet, R_p is the planetary radius, and τ is the optical depth from the planetary surface to space, parallel to the surface normal vector. See Appendix D for a derivation of this expression. For an airless planet with a surface albedo of unity, one recovers that $F_{\text{refl}} = (2/3)F_*(R_p/d)^2$, hence a geometric albedo of $2/3$, as expected.

The corresponding high-resolution emission and reflection spectra for an Earth-like Proxima Cen b are shown in the right panel of Figure 10 for the relevant wavelength range of 3.6 to 3.8 μm . As is evident from the right panel of Figure 10, the reflected flux is favorable over the emitted by a factor ~ 15 . Since this is a function of the albedo, the various available choices of the latter are discussed at below. Moreover, more and deeper lines appear to be visible in the reflected spectrum when compared to the emission spectrum. This can be understood from the fact that in the emission case isothermal regions in the P - T structure tend to decrease the line contrasts, whereas in the reflection case stellar light is simply attenuated as it moves through the planet's atmosphere. Note that the full observed planetary spectrum is simply the sum of the reflected and emitted flux, due to the linear nature of the radiative transfer equation.

Our SNR prediction, using Equation 5, suggests that HDO can be detected (at 5σ) if a planet spectrum can be obtained with an SNR per pixel of 0.23 and 0.11 for the emitted and reflected components, respectively. Making use of Equation 6, we calculate that a single night (10 hr) of ELT *METIS* observations should result in an SNR of ~ 0.1 per pixel, when observed in reflected light and assuming a stellar flux reduction at the planet position of a factor $f=1000$. This suggests that if Proxima Cen b is an Earth twin and is similarly enriched in deuterium, HDO could be detectable in ~ 1 night of observations. However, it will have to be seen how well ELT coronagraphy will work at only $1.8 \lambda/D$, the star-planet separation at longest elongation. Assuming a maximum practical integration time of 10 nights, a minimum star-light suppression of $f = 100$ needs to be achieved to detect HDO in Proxima Cen b. Note that we neglected the phase illumination of the planet, assuming full visibility of the planet dayside. If only half of the visible hemisphere of the planet is illuminated by the star during observations, the required observing time increases by a factor 4.

We stress possible limitations of our study. First on the non-exhaustive list of effects that should be included in future studies, is the choice of the surface albedo, which was taken to be 30 %. This is the bolometric value expected for ice or snow when considering an M-dwarf host star (Turbet et al. 2016). For comparison, ice and snow on Earth have an albedo of ~ 60 %, desert sand has ~ 40 %, whereas oceans and vegetation have albedos

of about 5 and 15 %, respectively (see, e.g., Table 2.2 in Marshall & Plumb 2007). Next, one may consider the effect of scattering the stellar light in the atmosphere itself, and Turbet et al. (2016) found that the local bolometric albedo for Proxima Cen b may increase from 30 % (ice/snow) to 50 % in regions where water clouds may form. This adds the effect of clouds to the list of processes not considered here. Increasing the albedo due to clouds may seem like an advantage, because a higher albedo increases the reflected flux. At the same time, if the majority of the reflection flux stems from water clouds, then the sharp lines of the water vapor opacity will weaken, as the vapor-richest regions are hidden below the clouds. Of course, using an Earth atmosphere to model the HDO detectability should be kept in mind as an important limitation, because Proxima Cen b's atmospheric temperature and chemical abundance structure could be very different from what was assumed here.

7. Summary and outlook

In this paper we have studied the potential of detecting the $^{13}\text{C}^{16}\text{O}$, HDO, and CH_3D isotopologues in exoplanet atmospheres using ground-based high-dispersion spectroscopy. For the $^{13}\text{C}^{16}\text{O}$ case we considered the dayside emission spectra of hot Jupiters, while concentrating on self-luminous planets for the HDO and CH_3D isotopologues. In addition, a HDO reflection study was carried out for Proxima Cen b. In particular the HDO and CH_3D isotopologues are interesting, since their detection will lead to constraints on atmospheric D/H ratios, providing insights to planet accretion histories and possible atmospheric evaporation processes. In addition, for massive substellar objects, constraints on the D/H ratio may shed light on their possible deuterium burning history, and hence mass.

We expect that $^{13}\text{C}^{16}\text{O}$ will be readily detectable with instruments such as *CRILES+* on the VLT. Particularly observations in the 4.7 micron range, in the CO fundamental band, will lead to high detection SNRs for $^{13}\text{C}^{16}\text{O}$, with only a few nights of observations.

Excitingly, HDO will be detectable at 3.7 μm with the ELTs over a broad range of atmospheric temperatures. Since methane tends to blanket the HDO features, atmospheres in which methane is quenched may be significantly more accessible, potentially even with 10m class telescopes. If sufficient coronagraphic starlight reduction can be reached with *METIS* on the ELT at $2\lambda/D$, an HDO detection in Proxima b will be possible, if its atmosphere is water rich and Earth-like.

The CH_3D isotopologue, the detection of which will also constrain the D/H ratio in a planet atmosphere, could in the most favourable cases be in reach of 10m class telescopes, for planets in a temperature range more limited than in the case of HDO due to an expected lack of methane in the hotter planets.

Isotopologues will soon be a part of the exoplanet characterisation tools. Here we studied only three isotopologues, $^{13}\text{C}^{16}\text{O}$, HDO, and CH_3D , and only consider the signal strength they imprint onto the observed planet spectra. Future studies should also consider different molecules, look into different techniques such as transmission spectroscopy (which we avoided due to the high uncertainty of their cloud and haze properties), and most importantly try to answer how well one can retrieve the actual isotopologue abundance (ratios) from high-resolution observations. The question is whether such observations must be complemented by lower resolution spectroscopy to better constrain, e.g., the atmospheric temperature profile. Another unanswered question is whether current line lists have the required precision for carrying out such studies. If line positions of any important atmo-

spheric absorber are wrong, or lines are missing altogether, then the noise arising from pseudo-random line overlap between the observations and models may make the successful isotopologue detection more difficult when using the cross-correlation technique. Striving for the detection of isotopologues in exoplanet atmospheres will challenge the exoplanet modeling community to refine their modeling and retrieval techniques.

Acknowledgements. P.M. thanks J. Kasting and R. Pierrehumbert for helpful discussions. P.M. also thanks C. Morley and M. Line, whose comments greatly improved the quality of this work. This work benefited from the 2018 Exoplanet Summer Program in the Other Worlds Laboratory (OWL) at the University of California, Santa Cruz, a program funded by the Heising-Simons Foundation. P.M. and I.S. acknowledge support from the European Research Council under the European Unions Horizon 2020 research and innovation programme under grant agreement No. 694513.

References

- Ali-Dib, M., Mousis, O., Petit, J.-M., & Lunine, J. I. 2014, *ApJ*, 785, 125 [1.1](#)
- Altwegg, K., Balsiger, H., Bar-Nun, A., et al. 2015, *Science*, 347, 1261952 [1.1](#)
- Altwegg, K. & Bockelée-Morvan, D. 2003, *Space Sci. Rev.*, 106, 139 [1.1](#)
- Anglada-Escudé, G., Amado, P. J., Barnes, J., et al. 2016, *Nature*, 536, 437 [6](#)
- Asplund, M., Grevesse, N., Sauval, A. J., & Scott, P. 2009, *ARA&A*, 47, 481 [1](#)
- Ayres, T. R., Lyons, J. R., Ludwig, H.-G., Caffau, E., & Wedemeyer-Böhm, S. 2013, *ApJ*, 765, 46 [1](#)
- Baraffe, I., Chabrier, G., Barman, T. S., Allard, F., & Hauschildt, P. H. 2003, *A&A*, 402, 701 [4](#)
- Barber, R. J., Tennyson, J., Harris, G. J., & Tolchenov, R. N. 2006, *MNRAS*, 368, 1087 [3](#)
- Baudino, J.-L., Bézard, B., Boccaletti, A., et al. 2015, *A&A*, 582, A83 [2.1](#)
- Baudino, J.-L., Mollière, P., Venot, O., et al. 2017, *ApJ*, 850, 150 [2.1](#)
- Béjar, V. J. S., Osorio, M. R. Z., & Rebolo, R. 1999, *ApJ*, 521, 671 [4](#)
- Bigg, G. R. 2004, *The Oceans and Climate*, 286 [6](#)
- Birkby, J. L., de Kok, R. J., Brogi, M., et al. 2013, *MNRAS*, 436, L35 [1](#)
- Birkby, J. L., de Kok, R. J., Brogi, M., Schwarz, H., & Snellen, I. A. G. 2017, *AJ*, 153, 138 [1](#)
- Biver, N., Moreno, R., Bockelée-Morvan, D., et al. 2016, *A&A*, 589, A78 [1.1](#)
- Bodenheimer, P., D'Angelo, G., Lissauer, J. J., Fortney, J. J., & Saumon, D. 2013, *ApJ*, 770, 120 [4](#)
- Borysow, A. & Frommhold, L. 1989, *ApJ*, 341, 549 [2.1](#)
- Borysow, A., Frommhold, L., & Moraldi, M. 1989, *ApJ*, 336, 495 [2.1](#)
- Brandl, B. R., Feldt, M., Glasse, A., et al. 2014, in *Proc. SPIE*, Vol. 9147, Ground-based and Airborne Instrumentation for Astronomy V, 914721 [1](#), [4.3](#)
- Brogi, M., de Kok, R. J., Birkby, J. L., Schwarz, H., & Snellen, I. A. G. 2014, *A&A*, 565, A124 [1](#), [1.3](#), [3.2](#), [3.3](#), [4](#), [3.4](#), [3.4](#)
- Brogi, M., Snellen, I. A. G., de Kok, R. J., et al. 2012, *Nature*, 486, 502 [1](#), [3.2](#)
- Bryan, M. L., Benneke, B., Knutson, H. A., Batygin, K., & Bowler, B. P. 2018, *Nature Astronomy*, 2, 138 [1](#)
- Burrows, A., Hubbard, W. B., Lunine, J. I., & Liebert, J. 2001, *Reviews of Modern Physics*, 73, 719 [4](#)
- Chabrier, G. & Baraffe, I. 2000, *ARA&A*, 38, 337 [4](#)
- Chan, Y. M. & Dalgarno, A. 1965, *Proceedings of the Physical Society*, 85, 227 [2.1](#)
- Charbonneau, D., Berta, Z. K., Irwin, J., et al. 2009, *Nature*, 462, 891 [4.3](#)
- Clarke, J. T., Mayyasi, M., Bhattacharyya, D., et al. 2017, *Journal of Geophysical Research (Space Physics)*, 122, 2336 [1.2](#)
- Clayton, D. D. & Nittler, L. R. 2004, *ARA&A*, 42, 39 [1](#)
- Clayton, R. N. 1993, *Annual Review of Earth and Planetary Sciences*, 21, 115 [1.1](#)
- Cridland, A. J., Pudritz, R. E., & Alessi, M. 2016, *MNRAS*, 461, 3274 [1.1](#)
- Dalgarno, A. & Williams, D. A. 1962, *ApJ*, 136, 690 [2.1](#)
- de Bergh, C. 1995, *Advances in Space Research*, 15, 427 [5](#)
- De Bièvre, P., Gallet, M., Holden, N. E., & Barnes, I. L. 1984, *Journal of Physical and Chemical Reference Data*, 13, 809 [3.1](#), [E.1](#)
- de Kok, R. J., Brogi, M., Snellen, I. A. G., et al. 2013, *A&A*, 554, A82 [1](#)
- Feuchgruber, H., Lellouch, E., Orton, G., et al. 2013, *A&A*, 551, A126 [1.1](#)
- Follert, R., Dorn, R. J., Oliva, E., et al. 2014, in *Proc. SPIE*, Vol. 9147, Ground-based and Airborne Instrumentation for Astronomy V, 914719 [1](#), [4.3](#)
- Fu, Q. & Liou, K. N. 1992, *Journal of Atmospheric Sciences*, 49, 2139 [2.2](#)
- Garraffo, C., Drake, J. J., & Cohen, O. 2016, *ApJ*, 833, L4 [6](#)
- Geiss, J. & Reeves, H. 1981, *A&A*, 93, 189 [1.1](#)
- Ghosh, P. & Brand, W. A. 2003, *International Journal of Mass Spectrometry*, 228, 1 [1.2.1](#)
- Goody, R., West, R., Chen, L., & Crisp, D. 1989, *J. Quant. Spec. Radiat. Transf.*, 42, 539 [2.2](#)
- Guillot, T. & Gautier, D. 2014, *ArXiv e-prints* [1.1](#)
- Halbout, J., Mayeda, T. K., & Clayton, R. N. 1986, *Earth and Planetary Science Letters*, 80, 1 [1.1](#)
- Hanel, R. A., Conrath, B. J., Kunde, V. G., et al. 1972, *J. Geophys. Res.*, 77, 2629 [6](#)
- Harvey, A. H., Gallagher, J. S., & Levelt Sengers, J. M. H. 1998, *Journal of Physical and Chemical Reference Data*, 27, 761 [2.1](#)
- Hauschildt, P. H., Allard, F., & Baron, E. 1999, *ApJ*, 512, 377 [3.4](#), [4.3](#), [6](#)
- Helling, C., Woitke, P., Rimmer, P. B., et al. 2014, *Life*, volume 4, issue 2, pages 142-173, 4, 142 [1.1](#)
- Hill, C., Yurchenko, S. N., & Tennyson, J. 2013, *Icarus*, 226, 1673 [3](#)
- Hoeijmakers, H. J., Ehrenreich, D., Heng, K., et al. 2018, *ArXiv e-prints* [1](#)
- Howard, W. S., Tilley, M. A., Corbett, H., et al. 2018, *ArXiv e-prints* [6](#)
- Jakosky, B. M. & Phillips, R. J. 2001, *Nature*, 412, 237 [1.2](#)
- Jones, A., Noll, S., Kausch, W., Szyszka, C., & Kimeswenger, S. 2013, *A&A*, 560, A91 [3.1](#)
- Kervella, P., Thévenin, F., & Lovis, C. 2017, *A&A*, 598, L7 [6](#)
- Krasnopolsky, V. A. 2015, *Icarus*, 257, 377 [1.2](#)
- Kulikov, Y. N., Lammer, H., Lichtenegger, H. I. M., et al. 2006, *Planet. Space Sci.*, 54, 1425 [1.2](#)
- Kurucz, R. 1993, *SYNTHES Spectrum Synthesis Programs and Line Data*. Kurucz CD-ROM No. 18. Cambridge, Mass.: Smithsonian Astrophysical Observatory, 1993., 18 [2.1](#)
- Lacis, A. A. & Oinas, V. 1991, *J. Geophys. Res.*, 96, 9027 [2.2](#)
- Langmuir, C. & Broecker, W. 2012, *How to Build a Habitable Planet: The Story of Earth from the Big Bang to Humankind* (Princeton University Press) [1.2.1](#)
- Lellouch, E., Bézard, B., Fouchet, T., et al. 2001, *A&A*, 370, 610 [1.1](#)
- Leshin, L. A. 2000, *Geophys. Res. Lett.*, 27, 2017 [1.2](#)
- Linsky, J. L., Draine, B. T., Moos, H. W., et al. 2006, *ApJ*, 647, 1106 [1](#)
- Madhusudhan, N., Amin, M. A., & Kennedy, G. M. 2014, *ApJ*, 794, L12 [1.1](#)
- Madhusudhan, N., Bitsch, B., Johansen, A., & Eriksson, L. 2016, *ArXiv e-prints* [1.1](#)
- Mahaffy, P. R., Donahue, T. M., Atreya, S. K., Owen, T. C., & Niemann, H. B. 1998, *Space Sci. Rev.*, 84, 251 [1.1](#)
- Mancini, L., Giordano, M., Mollière, P., et al. 2016a, *MNRAS*, 461, 1053 [2.1](#)
- Mancini, L., Kemmer, J., Southworth, J., et al. 2016b, *MNRAS*, 459, 1393 [2.1](#)
- Mancini, L., Southworth, J., Raia, G., et al. 2017, *MNRAS*, 465, 843 [2.1](#)
- Marboeuf, U., Thiabaud, A., Alibert, Y., & Benz, W. 2018, *MNRAS*, 475, 2355 [1.1](#)
- Marboeuf, U., Thiabaud, A., Alibert, Y., Cabral, N., & Benz, W. 2014a, *A&A*, 570, A36 [1.1](#)
- Marboeuf, U., Thiabaud, A., Alibert, Y., Cabral, N., & Benz, W. 2014b, *A&A*, 570, A35 [1.1](#)
- Marshall, J. & Plumb, R. 2007, *Atmosphere, Ocean and Climate Dynamics: An Introductory Text*, International Geophysics (Elsevier Science) [6](#)
- Milam, S. N., Savage, C., Brewster, M. A., Ziurys, L. M., & Wyckoff, S. 2005, *ApJ*, 634, 1126 [1](#), [1.1](#)
- Miller, N. & Fortney, J. J. 2011, *ApJ*, 736, L29 [1.1](#)
- Mollière, P. & Mordasini, C. 2012, *A&A*, 547, A105 [4](#)
- Mollière, P., van Boekel, R., Bouwman, J., et al. 2017, *A&A*, 600, A10 [2.1](#), [1](#), [4.3](#), [6](#)
- Mollière, P., van Boekel, R., Dullemond, C., Henning, T., & Mordasini, C. 2015, *ApJ*, 813, 47 [2.1](#), [2.2](#), [3.4](#), [4.3](#), [6](#)
- Morbidelli, A. 2005, *ArXiv Astrophysics e-prints* [1.1](#)
- Mordasini, C., van Boekel, R., Mollière, P., Henning, T., & Benneke, B. 2016, *ApJ*, 832, 41 [1.1](#), [2.1](#)
- Morley, C. V., Fortney, J. J., Kempton, E. M.-R., et al. 2013, *ApJ*, 775, 33 [4.3](#)
- Morley, C. V., Fortney, J. J., Marley, M. S., et al. 2015, *ApJ*, 815, 110 [4.3](#)
- Morley, C. V., Skemer, A. J., Allers, K. N., et al. 2018, *ArXiv e-prints* [5](#)
- Noll, S., Kausch, W., Barden, M., et al. 2012, *A&A*, 543, A92 [3.1](#)
- Nugroho, S. K., Kawahara, H., Masuda, K., et al. 2017, *AJ*, 154, 221 [1](#)
- Öberg, K. I. & Bergin, E. A. 2016, *ApJ*, 831, L19 [1.1](#)
- Öberg, K. I., Murray-Clay, R. A., & Bergin, E. A. 2011, *ApJ letters*, 743, L16 [1.1](#)
- Owen, T. & Encrenaz, T. 2003, *Space Sci. Rev.*, 106, 121 [5](#)
- Pavlenko, Y. V., Harris, G. J., Tennyson, J., et al. 2008, *MNRAS*, 386, 1338 [4](#)
- Pearson, V. K., Sephton, M. A., Franchi, I. A., Gibson, J. M., & Gilmour, I. 2006, *Meteoritics and Planetary Science*, 41, 1899 [1.1](#)
- Piskorz, D., Benneke, B., Crockett, N. R., et al. 2016, *ApJ*, 832, 131 [1](#)
- Piskorz, D., Benneke, B., Crockett, N. R., et al. 2017, *AJ*, 154, 78 [1](#)
- Piskunov, N. E., Kupka, F., Ryabchikova, T. A., Weiss, W. W., & Jeffery, C. S. 1995, *A&AS*, 112, 525 [2.1](#)
- Polehampton, E. T., Baluteau, J.-P., & Swinyard, B. M. 2005, *A&A*, 437, 957 [1](#)
- Quay, P. D., King, S. L., Stutsman, J., et al. 1991, *Global Biogeochemical Cycles*, 5, 25 [1.2.1](#)
- Rajan, A., Rameau, J., De Rosa, R. J., et al. 2017, *AJ*, 154, 10 [F.1](#)

- Ribas, I., Bolmont, E., Selsis, F., et al. 2016, *A&A*, 596, A111 [6](#)
- Richard, C., Gordon, I. E., Rothman, L. S., et al. 2012, *J. Quant. Spec. Radiat. Transf.*, 113, 1276 [2.1](#)
- Rodler, F., Kürster, M., & Barnes, J. R. 2013, *MNRAS*, 432, 1980 [1](#)
- Rodler, F., Lopez-Morales, M., & Ribas, I. 2012, *ApJ*, 753, L25 [1](#)
- Romano, D., Matteucci, F., Zhang, Z.-Y., Papadopoulos, P. P., & Ivison, R. J. 2017, *MNRAS*, 470, 401 [1](#), [1.1](#)
- Rothman, L. S., Gordon, I. E., Babikov, Y., et al. 2013, *J. Quant. Spec. Radiat. Transf.*, 130, 4 [2.1](#)
- Rothman, L. S., Gordon, I. E., Barber, R. J., et al. 2010, *J. Quant. Spec. Radiat. Transf.*, 111, 2139 [2.1](#)
- Samland, M., Mollière, P., Bonnefoy, M., et al. 2017, *A&A*, 603, A57 [2.1](#), [4.1](#), [F.1](#)
- Santos, N. C., Israelian, G., & Mayor, M. 2004, *A&A*, 415, 1153 [1](#)
- Saumon, D., Hubbard, W. B., Burrows, A., et al. 1996, *ApJ*, 460, 993 [4](#)
- Ségransan, D., Kervella, P., Forveille, T., & Queloz, D. 2003, *A&A*, 397, L5 [6](#)
- Skemer, A. J., Morley, C. V., Allers, K. N., et al. 2016, *ApJ*, 826, L17 [5](#)
- Sneep, M. & Ubachs, W. 2005, *J. Quant. Spec. Radiat. Transf.*, 92, 293 [2.1](#)
- Snellen, I., de Kok, R., Birkby, J. L., et al. 2015, *A&A*, 576, A59 [4.2](#), [4.3](#)
- Snellen, I. A. G., Brandl, B. R., de Kok, R. J., et al. 2014, *Nature*, 509, 63 [1](#)
- Snellen, I. A. G., de Kok, R. J., de Mooij, E. J. W., & Albrecht, S. 2010, *Nature*, 465, 1049 [1](#)
- Southworth, J., Mancini, L., Madhusudhan, N., et al. 2017, *AJ*, 153, 191 [2.1](#)
- Tennyson, J. & Yurchenko, S. N. 2012, *MNRAS*, 425, 21 [2.1](#)
- Thiabaud, A., Marboeuf, U., Alibert, Y., et al. 2014, *A&A*, 562, A27 [1.1](#)
- Thorngren, D. P., Fortney, J. J., Murray-Clay, R. A., & Lopez, E. D. 2016, *ApJ*, 831, 64 [1.1](#)
- Tinney, C. G., Butler, R. P., Marcy, G. W., et al. 2001, *ApJ*, 551, 507 [3](#)
- Tremblin, P., Amundsen, D. S., Mourier, P., et al. 2015, *ApJ*, 804, L17 [2.1](#)
- Turbet, M., Leconte, J., Selsis, F., et al. 2016, *A&A*, 596, A112 [6](#), [6](#)
- Villanueva, G. L., Mumma, M. J., Novak, R. E., et al. 2015, *Science*, 348, 218 [1.2](#), [4](#)
- Voronin, B. A., Tennyson, J., Tolchenov, R. N., Lugovskoy, A. A., & Yurchenko, S. N. 2010, *MNRAS*, 402, 492 [3](#)
- Wittenmyer, R. A., Endl, M., & Cochran, W. D. 2007, *ApJ*, 654, 625 [1](#)
- Yurimoto, H., Kuramoto, K., Krot, A. N., et al. 2007, *Protostars and Planets V*, 849 [1.1](#)
- Zahnle, K. J. & Marley, M. S. 2014, *ApJ*, 797, 41 [4.1](#), [5](#)

Appendix A: Cross-correlation signal-to-noise

A.1. Lines of equal strength

Here we derive the signal-to-noise characteristics when trying to identify a line species in noisy data. We start with the case of spectral lines which all have the same strength in the spectral data. The cross-correlation is defined as

$$(f * g)(\tau) = \int_{-\infty}^{\infty} f^*(t)g(t + \tau)dt, \quad (\text{A.1})$$

it is thus the integral of the product of the function f and the function g , where g has been shifted to the “left” (i.e. towards more negative t values) by the distance τ . For real valued functions it holds that $(f * g)(\tau) = (g * f)(-\tau)$.

We now consider a planetary spectrum observed at high resolution within a spectral range $[-\nu, \nu]$. Here we assume that we have a perfect model for the noise-free spectrum of the planet, $f(\nu)$. However, the observation will not give $f(\nu)$, it will give the planetary spectrum plus noise $n(\nu)$. The total observed signal is then $o(\nu) = f(\nu) + n(\nu)$. Throughout this section, for clarity, we will describe the noise assuming a Gaussian with a mean value of zero, and we assume that the planetary spectrum is zero outside the lines, while the lines are assumed to be positive. Because we expect the noise to be fully dominated by the planet’s host star, assuming Gaussian-distributed noise is appropriate, as the Poisson distribution transitions to a Gauss distribution at large mean values. Assuming that the noise has a constant standard deviation σ for every pixel, a single line within the planetary spectrum, of strength I , will only be visible if $I \gg \sigma$. Moreover,

the signal-to-noise ratio (SNR) of a single line observation will be $\text{SNR}_{\text{single}} = I/\sigma$.

Now, instead, we carry out a cross-correlation between the observation and the model spectrum, across the range where we have data:

$$\begin{aligned} (o * f)(\nu_0) &= \int_{-\nu}^{\nu} [f(\nu) + n(\nu)] f(\nu + \nu_0) d\nu \\ &= \int_{-\nu}^{\nu} f(\nu) f(\nu + \nu_0) d\nu + \int_{-\nu}^{\nu} n(\nu) f(\nu + \nu_0) d\nu. \end{aligned} \quad (\text{A.2})$$

$$(\text{A.3})$$

Here we neglect the complex conjugate notation, as all functions are real-valued. If one has a perfect (in reality: good) model, then the first integral in Equation (A.3) will be maximal for $\nu_0 = 0$. We call this value the signal S . This is the signal to be extracted by means of cross-correlation. If the planet has a density of ρ lines per frequency interval in the observed spectral region, with all lines of roughly equal strength I , then the height of the peak S at $\nu_0 = 0$ can be approximated as

$$S = \int_{-\nu}^{\nu} f(\nu) f(\nu) d\nu \approx 2\nu\rho I^2 \Delta\nu, \quad (\text{A.4})$$

where $\Delta\nu$ is the approximate line width of the lines within the studied frequency range and $2\nu\rho$ is the number of lines probed across $[-\nu, \nu]$. The second integral in Equation (A.3), which we will call noise N , can be approximated by noticing that the integral will be dominated by the locations where $f(\nu + \nu_0)$ is maximal (i.e. where the lines are). The mean value, for arbitrary ν_0 (assuming that the properties of the planet lines stay constant across the range probed by shifting ν_0) can hence be written as

$$N = \int_{-\nu}^{\nu} n(\nu) f(\nu + \nu_0) d\nu \approx \sum_{i=1}^{2\nu\rho} I \sigma_i \Delta\nu. \quad (\text{A.5})$$

Here, σ_i denotes an actual sampled value of the noise with standard deviation σ . Now, because we assume the noise values to be independent and random (following a Poisson distribution), we find that

$$N \approx I \sigma \Delta\nu \sqrt{2\nu\rho}. \quad (\text{A.6})$$

The SNR measured at the peak of the cross-correlation function of model and observation is thus

$$\frac{S}{N} = \sqrt{2\nu\rho} \frac{I}{\sigma}, \quad (\text{A.7})$$

and one sees that the SNR grows with the square root of the number of lines being probed.

In reality the data will contain not only the planetary signal, and the photon noise of the observation, but also lines belonging to the planet’s host star, telluric lines, or planetary lines not included in the model $f(\nu)$. If these contaminant lines are uncorrelated with respect to the distribution of the lines in the model spectrum, then they merely correspond to an additional noise source. If this is not the case, and there is some non-negligible correlation, then this will be visible in the form of secondary peaks in the cross-correlation function.

A.2. Lines of varying strength

If every line i has a different strength I_i , then the signal in the first term of Equation A.3 can be approximated as

$$S = \sum_{i=1}^{N_{\text{lines}}} I_i^2 \Delta\nu, \quad (\text{A.8})$$

whereas for the noise it holds that

$$N = \sum_{i=1}^{N_{\text{lines}}} I_i \sigma_i \Delta \nu. \quad (\text{A.9})$$

Because the noise values at the N_{lines} line positions are independent, it holds that

$$N = \sigma \Delta \nu \left(\sum_{i=1}^{N_{\text{lines}}} I_i^2 \right)^{1/2}. \quad (\text{A.10})$$

Thus it holds that

$$\frac{S}{N} = \frac{1}{\sigma} \left(\sum_{i=1}^{N_{\text{lines}}} I_i^2 \right)^{1/2}. \quad (\text{A.11})$$

Hence, the strongest lines will be most important. Moreover, when evaluating Equation A.11 for estimating the expected signal-to-noise for a given model $f(\nu) = I(\nu)$, and a given noise level σ , one can simply set

$$\frac{S}{N} = \frac{1}{\sigma} \left(\sum_{i=1}^{N_{\nu}} I_i^2 \right)^{1/2}, \quad (\text{A.12})$$

i.e. taking the sum over all frequency points, rather than just the line positions.

Appendix B: Testing the cross-correlation SNR approximation (Equation 5) for trace species

B.1. Testing the SNR approximation for HDO

Here we present full simulations of the HDO detection for the self-luminous, directly imageable planets, as described in Sections 4.1. This is done to validate our approximative SNR calculations (see Equation 5) used for the HDO detection in sections 4 and 6. “Full simulation” here means that we included telluric absorption, added photon noise, and then carried out a synthetic reduction step, followed by cross-correlating with an HDO model.

For the full simulation we first obtained synthetic observations as described in Section 2.3. As before, we assumed to record the data as 100 individual spectra, at a resolution of 10^5 , and three wavelength steps per resolution element.⁵ Our benchmark calculations are for young, directly imaged planets, and we therefore assumed that the star-light at the planet’s position is reduced by a factor of $f = 1000$. Similar to the CO detection study (see Section 3), we treated the stellar flux as featureless, assuming any features can be readily removed. For the velocity offset between the telluric absorption and the planet–star system we assumed a value of 30 km/s, which for all systems near the ecliptic can be achieved due to the barycentric motion of the Earth.

Here we will analyse the characteristics of the HDO detection SNR in planets as a function of T_{equ} at a very large signal-to-noise level, and compare this to the prediction made with the approximation enabled by Equation 5, described in Section 4.2. We chose to work with a high signal-to-noise, in order to be able to compare the full and approximative methods properly, otherwise

⁵ Assuming 100 individual spectra is not strictly needed, because the planet’s orbital motion is no longer used to remove the tellurics, but we kept this parameter constant when transitioning from the model for hot Jupiters to the self-luminous gas giant observations.

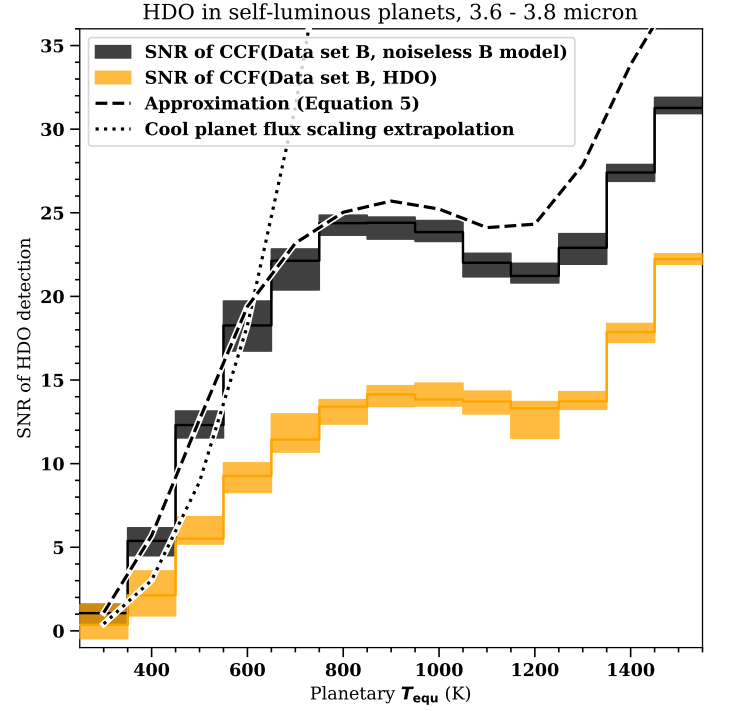


Fig. B.1. SNR of the HDO detection in the spectrum of a directly imaged gas planet as a function of the planetary T_{equ} . The HDO/H₂O ratio was 4×10^{-5} . Here we assumed $\text{SNR}_{*,@3.7\mu\text{m}} = 3317$ per spectrum, a stellar flux 1000 times smaller at the position of the planet, considering 100 spectral observations. Orange boxes: detection SNR when correlating the contaminant removed observation (data set B) with a pure HDO isotopologue template. Black boxes: detection SNR when correlating with the noiseless, telluric-free model B spectrum. The box height corresponds to the measured 16 and 84 percentiles of the measured SNRs, when running the simulation multiple times. The black dotted line denotes the SNR scaling expected purely from the increasing planet–star contrast as the planet becomes hotter. This assumes that the ratio of the HDO and H₂O opacities is not temperature dependent. The black dashed line shows the prediction of the SNR signal following Equation 5, indicating good agreement.

most of the cases would simply lead to non-detections, with the SNRs scattering around zero. The calculations here assume that at the location of the star the spectral single-pixel SNR at $2.3 \mu\text{m}$ is $\text{SNR}_*(2.3 \mu\text{m}) = 5000$ per single spectrum (we will evaluate 100 spectra later), leading to $\text{SNR}_* = 3317$ at $3.7 \mu\text{m}$ (assuming a sun-like host star). Identically to Section 3.1, Equation 4, we use a stellar flux model to calculate the corresponding stellar SNR_* at $3.7 \mu\text{m}$. Moreover, because we assume that at the location of the planet the stellar flux is lower by a factor 1000, the photon noise is lower by a factor $\sqrt{1000}$. The data reduction process is described in Appendix B.2.

The results for the HDO detection SNR are shown in Figure B.1. We show both the SNRs obtained for cross-correlating the synthetic observation with a pure HDO isotopologue template spectrum (i.e. taking the full self-consistent atmospheric structure but considering only the HDO opacity for the spectrum), and the detection SNR obtained when using the better cross-correlation model $F_P - F_{P-\text{HDO}}$, which will have the HDO line ratios at correct relative strength. This corresponds to the noiseless and telluric-free model of data set B, described in Section

3.2. The synthetic observation we correlated the models with was the contaminant corrected data set, analogous to data set B in Figure 1. The cross-correlation functions of the 100 synthetic observations we added before calculating the detection SNR. As is evident, using the noiseless and telluric-free model for data set B, instead of the pure HDO isotopologue template spectrum, gives a SNR which is on average better by $\Delta\text{SNR} \sim 7$.

It can be seen that the detection SNR first increases with temperature, in a way which we find to be linear in the increasing planet–star contrast (black dotted line in Figure B.1) at $3.7 \mu\text{m}$, as expected, as the planet becomes hotter. From $T_{\text{equ}} \approx 700 \text{ K}$ on this behavior stops and the SNR stagnates, due to the fact the HDO opacity is weaker with respect to the H_2O opacity at high temperatures. For higher $T_{\text{equ}} \gtrsim 1200 \text{ K}$ the HDO detection SNR starts rising again. This is caused by methane, the main absorber in the $3.7 \mu\text{m}$ atmospheric window, being less abundant at higher temperatures (see the discussion of Figure 7 in Section 4.4).

The black dashed line in Figure B.1 shows the predicted detection SNR results when using Equation 5. For the spectral signal-to-noise per pixel, used in Equation 5, we evaluated

$$(S/N)_{\text{pix}} = \frac{c}{\sqrt{1/f + c}} \cdot \text{SNR}_*(3.7 \mu\text{m}), \quad (\text{B.1})$$

where $f = 1000$ is the flux stellar flux reduction at the position of the planet, and c is the mean planet to star contrast in the wavelength region of interest.

This makes use of our estimate from Appendix B.2, namely that the data reduction process itself is not expected to increase the error of the final spectrum of the target species considerably. One expects Equation 5 to follow the detection SNR for cross-correlating the observation with the noiseless and telluric-free model for data set B, and indeed the agreement is very good until equilibrium temperatures of 1100 K . Then Equation 5 starts to slightly overpredict the detection SNR. We do not attribute this to the failing of Equation 5 at these higher temperatures. Rather, we suspect that the detailed simulation of the HDO detection, which we compare to here, may give rise to additional noise. Note that the noise-free auto-correlation we calculate for the telluric-free data set B is even higher (≈ 45 in this temperature range), i.e. cannot be the reason for the SNR differences we observe here. The SNR approximation method (Equation 5) has thus been verified successfully.

B.2. Data reduction and estimated error magnitude

Here we describe the data reduction used in Appendix B.1, and discuss the resulting magnitude of the planet flux error bars, for a single spectral pixel.

For every of the 100 individual spectra considered here, the observed flux at the Earth’s surface is

$$F_{\text{surf}} = \mathcal{T}(F_* + F_{\text{P}}), \quad (\text{B.2})$$

where \mathcal{T} is the telluric transmission, F_* the stellar flux at the location of the planet, and F_{P} is the planet’s flux (planet and star are velocity-shifted with respect to the telluric transmission). The model input error of a single-pixel and spectrum is supposed to be constant in the approximation here, and given by

$$\Delta F_{\text{surf}} = \sigma. \quad (\text{B.3})$$

The telluric transmission model (also see Section 3.2) will be constructed by observing the star directly, i.e. not at the location

of the planet. We assume that the star, when observed directly, is brighter by a factor f . Hence the estimate of the telluric transmission, if assuming that the star’s flux without telluric absorption, F_* , is perfectly known, is:

$$\tilde{\mathcal{T}} = \frac{\langle \mathcal{T} f F_* \rangle_{\text{surf}}}{f F_*} \quad (\text{B.4})$$

where $\langle \mathcal{T} f F_* \rangle_{\text{surf}}$ is the median observed flux in a given pixel, taking all 100 spectra into account. Because the star is brighter by a factor f when observed directly, with the error scaling with \sqrt{f} , we find that

$$\Delta \tilde{\mathcal{T}} = \frac{1}{10 \sqrt{f}} \frac{\sigma}{F_*}, \quad (\text{B.5})$$

where the factor $1/10$ stems from combining the 100 spectra to get the transmission estimate. Now, using the measured transmission model, the model flux, taking into account the contaminant species only, is subtracted from the observation (see Section 3.2), leading to

$$F_{\text{rem}} = F_{\text{surf}} - \tilde{\mathcal{T}} F_{\text{P-HDO}} \quad (\text{B.6})$$

$$\approx \mathcal{T}[F_* + (F_{\text{P}} - F_{\text{P-HDO}})] \quad (\text{B.7})$$

The expected error then works out to be

$$\Delta F_{\text{rem}} = \sigma \sqrt{1 + \frac{1}{100f} \left(\frac{F_{\text{P-HDO}}}{F_*} \right)^2} \approx \sigma. \quad (\text{B.8})$$

Next, we remove the telluric lines, in order to not be dominated by these in the cross-correlation function:

$$F_{\text{remove tell}} = \frac{F_{\text{rem}}}{\tilde{\mathcal{T}}} \approx F_* + F_{\text{P}} - F_{\text{P-HDO}}. \quad (\text{B.9})$$

The error works out to be

$$\Delta F_{\text{remove tell}} = \sqrt{\left(\frac{\sigma}{\tilde{\mathcal{T}}} \right)^2 + \left(\frac{1}{10 \sqrt{f}} \frac{\sigma}{F_*} \frac{F_{\text{rem}}}{\tilde{\mathcal{T}}^2} \right)^2} \quad (\text{B.10})$$

$$= \frac{\sigma}{\tilde{\mathcal{T}}} \sqrt{1 + \frac{1}{100f} \left(\frac{F_{\text{rem}}}{F_*} \frac{1}{\tilde{\mathcal{T}}} \right)^2} \quad (\text{B.11})$$

$$\approx \frac{\sigma}{\tilde{\mathcal{T}}} \sqrt{1 + \frac{1}{100f}} \quad (\text{B.12})$$

$$\approx \frac{\sigma}{\tilde{\mathcal{T}}}. \quad (\text{B.13})$$

Note that we implicitly assumed here that the errors introduced by the transmission model estimate $\tilde{\mathcal{T}}$, when obtaining F_{rem} , and then $F_{\text{remove tell}}$, are independent. Only then would it be allowed to carry out two consecutive, and independent error propagation analyses. However, the error introduced by $\tilde{\mathcal{T}}$ is negligible in both steps, and the same would result from a more correct analysis.

Finally, we remove the influence of very strong telluric lines by setting (see Section 3.2, step 3)

$$F_{\text{final}} = \frac{1}{\sigma_{\text{column}}} \left(\frac{F_{\text{remove tell}}}{\langle \langle F_{\text{remove tell}} \rangle \rangle} - 1 \right), \quad (\text{B.14})$$

where $\langle \langle F_{\text{remove tell}} \rangle \rangle$ denotes the average over all spectral channels and all 100 spectra, and σ_{column} is the standard flux deviation of a given spectral channel, when considering all $F_{\text{remove tell}} / \langle \langle F_{\text{remove tell}} \rangle \rangle$ values for all 100 spectra. Hence, if

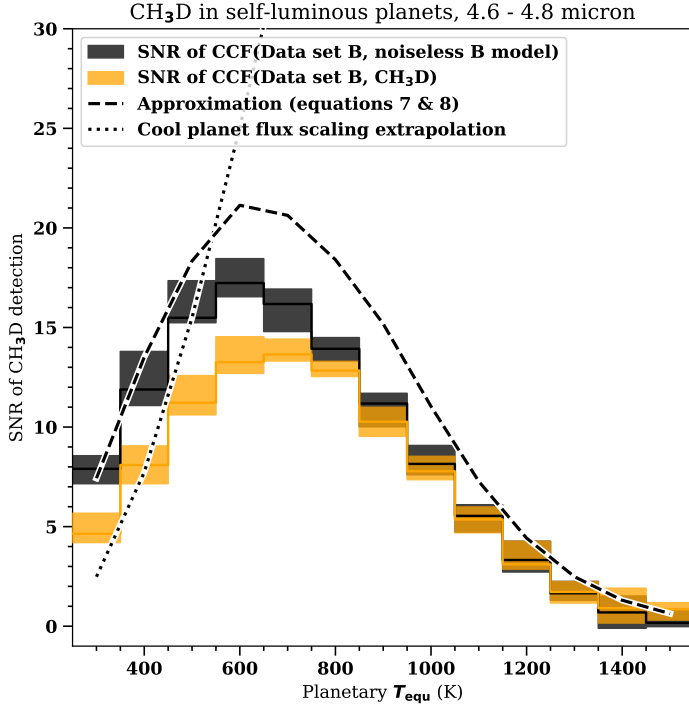


Fig. C.1. Analogous to Figure B.1, but this time testing the SNR-approximation (equations 7 and 8) for CH₃D.

there was no HDO line signal, then F_{final} would be simply a flat spectrum around zero, with a standard deviation of 1. One finally gets

$$\Delta F_{\text{final}} = \frac{1}{\sigma_{\text{column}}} \frac{\Delta F_{\text{remove tell}}}{\langle \langle F_{\text{remove tell}} \rangle \rangle} \quad (\text{B.15})$$

such that the expected signal-to-noise on the HDO-associated planetary flux per spectral pixel is

$$\frac{S}{N} = \tilde{\mathcal{F}} \frac{F_{\text{P}} - F_{\text{P-HDO}}}{\sigma}. \quad (\text{B.16})$$

The step for obtaining F_{final} (i.e. dividing by σ_{column}) will effectively remove the wavelength regions of strong telluric lines from the analysis. If one assumes that σ itself scales with $\mathcal{T}^{1/2}$, one gets the expected behaviour for photon noise, namely that the SNR of the observation scales with $\mathcal{T}^{1/2}$.

Hence, the reduction and contaminant removal step is not a significant noise source, with the total SNR given simply by the flux difference due to the target species, divided by the observational uncertainties.

Appendix C: Testing the SNR approximation for CH₃D

In Figure C.1 we show the test of the SNR-approximation for CH₃D (equations 7 and 8 in Section 5), analogous to the test shown for HDO in Figure B.1. One sees that we can reach a good agreement, with differences never larger than 30 %.

Appendix D: Derivation of the reflected flux as a function of surface albedo and atmospheric absorption

The reflected flux seen by an observer, viewing the dayside of a planet, can be expressed as

$$F_{\text{refl}} = \int I_{\text{refl}}(\Omega) \underbrace{(\mathbf{n}_{\text{P}} \cdot \mathbf{n}_{\text{detect}})}_1 d\Omega, \quad (\text{D.1})$$

where I_{refl} is the intensity of the reflected ray at the top of the exoplanet's atmosphere, $\mathbf{n}_{\text{detect}}$ is the normal vector of the detector, and \mathbf{n}_{P} is the direction of travel of the reflected light. Because of the large distances between observer and planet, the angle between the two vectors is negligibly small. Neglecting the atmospheric attenuation, the intensity of the scattered light at the surface of the planet can be found by equating

$$F_*(\lambda) \cos(\vartheta) = \pi I_{\text{refl}}(\lambda), \quad (\text{D.2})$$

such that

$$I_{\text{refl}}(\lambda) = \frac{\cos(\vartheta)}{\pi} F_*(\lambda), \quad (\text{D.3})$$

where ϑ is the angle between the normal vector of the planet's surface and the incoming radiation. Here it was assumed that the surface scatters isotropically, because for isotropic intensities it holds that $F = \pi I$, which follows from $F = \int I \cos(\vartheta) d\Omega$, integrated over a solid angle of 2π .

The area of an annulus on the planet's sphere, at an angle ϑ away from the substellar point, is

$$\Delta S = 2\pi R_{\text{P}} \sin(\vartheta) R_{\text{P}} \Delta\vartheta, \quad (\text{D.4})$$

where R_{P} is the planetary radius. The effective area seen by the observer is equal to $\cos(\vartheta) \Delta S$. Hence the total reflected flux, using $\Delta\Omega = \cos(\vartheta) \Delta S / d^2$ for the annulus' solid angle, where d is the distance between planet and observer, is

$$\begin{aligned} F_{\text{refl}}(\lambda) &= 2F_*(\lambda) \left(\frac{R_{\text{P}}}{d} \right)^2 \int_0^{\pi/2} \cos^2(\vartheta) \sin(\vartheta) d\vartheta \\ &= 2F_*(\lambda) \left(\frac{R_{\text{P}}}{d} \right)^2 \int_0^1 \mu^2 d\mu. \end{aligned} \quad (\text{D.5})$$

For a variable surface albedo $A(\lambda)$, as well as using that the ray will be attenuated by $e^{-\tau(\lambda)/\mu}$ twice as it travels through the atmosphere, one obtains

$$F_{\text{refl}}(\lambda) = 2A(\lambda) F_*(\lambda) \left(\frac{R_{\text{P}}}{d} \right)^2 \int_0^1 \mu^2 e^{-2\tau(\lambda)/\mu} d\mu, \quad (\text{D.6})$$

where $\tau(\lambda)$ is the optical depth of a ray from the planetary surface to space, running parallel to the normal vector of the planetary surface.

Appendix E: Nominal isotopologue abundances

In Table E.1 we list the default isotopologue ratios assumed in our calculations, if not otherwise noted in the text.

Appendix F: Parameters assumed for the planets in the HDO and CH₃ detection studies

In Table F.1 we list the parameters assumed for the planets in the HDO and CH₃D detection studies (sections 4 and 5).

Species	Relative abundance
H_2^{16}O	99.7 %
HD^{16}O	4×10^{-5}
H_2^{18}O	2×10^{-3}
H_2^{17}O	3.7×10^{-4}
HD^{18}O	6.2×10^{-8}
HD^{17}O	1.1×10^{-8}
$^{12}\text{C}^{16}\text{O}$	98.7 %
$^{13}\text{C}^{16}\text{O}$	1.1 %
$^{12}\text{C}^{18}\text{O}$	2×10^{-3}
$^{12}\text{C}^{17}\text{O}$	3.7×10^{-4}
$^{13}\text{C}^{18}\text{O}$	2.2×10^{-5}
$^{13}\text{C}^{17}\text{O}$	4.1×10^{-6}
CH_4	98.8%
CH_3D	8×10^{-5}

Table E.1. Default isotopologue ratios used in this study. The values were taken from the `molparam.txt` file of the HITRAN/HITEMP databases, which are based on the compilation of telluric isotopic abundances by De Bièvre et al. (1984). Because the Earth is 10-fold enriched in deuterium when compared to the mean galactic value, the relative abundances of D-bearing isotopologues were adjusted such that $\text{D}/\text{H} = 2 \times 10^{-5}$.

Name	T_* (K)	R_* (R_\odot)	T_p (K)	R_p (R_\oplus)	d (pc)
51 Eri b	7331 ^a	1.45 ^a	760 ^b	1.1 ^b	29.4
HR 8799 cde	7193	1.44	1200	1.05 ^c	39.4
GJ 504 b	5978	1.36	544	0.96	17.56
GJ 1214 b-like ^d	3250	0.22	604	0.25	7.28 ^d
51 Peg b	5793	1.27	1260	1.4 ^e	14.7

Table F.1. Parameters assumed for the planets in the HDO and CH_3D detection studies (sections 4 and 5). If not otherwise stated, the data shown here have been culled from <http://www.openexoplanetcatalogue.com>. References/notes: a: Rajan et al. (2017), b: Samland et al. (2017) c: the radii of HR 8799 cde are a mean value for the three planets, the radii of which vary between 1 and 1.1 R_\oplus . d: here we assume a planet and star similar in size and temperature to GJ 1214 b, but twice as close to the Solar System as the GJ 1214 system: for every transiting GJ 1214 b-like planet, one may expect up to 10 non-transiting ones, hence at least one at half the distance of the GJ 1214 system. e: this planet is non-transiting, hence its true radius is unknown. We assumed 1.4 R_\oplus here.